coatings

MDPI

Article

A Titanium-Based Superhydrophobic Coating with Enhanced Antibacterial, Anticoagulant, and Anticorrosive Properties for Dental Applications

Qin Rao, Ling Weng, Jinshuang Zhang, Yaqing Chen, Yujin Yang, Donghao Liu, Yurong Duan, Ying Cao *, Jialong Chen, Xiangyang Li, Hua Qiu, Quanli Li and Shunli Zheng *

College & Hospital of Stomatology, Anhui Medical University, Key Lab. of Oral Diseases Research of Anhui Province, Hefei 230032, China; chenyaqing7004@163.com (Y.C.)

* Correspondence: caoying0713@126.com (Y.C.); zhengshunli1986@126.com (S.Z.)

Abstract: Titanium and its alloys have been widely employed as dental implant materials. However, polymicrobial infection is still one of the most common reasons for implant failure, which has already become a worldwide problem and poses a threat to human health. In this study, a titanium-based (Ti-based) superhydrophobic coating was effectively created by anodization followed by hydrophobic modification of 1H,1H,2H,2H-perfluorodecyltriethoxysilane (FAS), which shows a high water contact angle (WCA) of 159.9 ± 5.8° and a low water sliding angle (WSA) of 2.7 ± 2.2°. The thickness of the anodized samples is from 500 nm to 4 μm as the anodizing voltage increases. The Ti-based superhydrophobic coating demonstrated the existence of Ti, O, C, F, and Si elements, and the corresponding phase compositions are Ti and anatase. The results showed that the Ti-based superhydrophobic coating has good biocompatibility to co-culture with L929 cells for 1, 3, and 5 days. It was also proven that the as-prepared Ti-based superhydrophobic coating has enhanced antibacterial abilities against *Staphylococcus aureus* (*S. aureus*) and *Porphyromonas gingivalis* (*P. gingivalis*, *P.g*) after 4, 12, and 24 h. Moreover, the Ti-based superhydrophobic coating can significantly reduce platelet adhesion and activation. In addition, the Ti-based superhydrophobic coating also exhibits a considerable positive shift in the corrosion potential (E_{corr}) and a decline of one order of magnitude in the corrosion current density (J_{corr}), showing good anticorrosive properties. It was also found that the capsule around the Ti-based superhydrophobic coating was thinner than that of bare Ti after implantation for 7, 15, and 28 days, indicating its good biosafety. Therefore, the as-prepared Ti-based superhydrophobic coating can be a suitable candidate for Ti-based implants in dental applications.

Keywords: titanium-based; superhydrophobic; anodization; antibacterial; anticoagulant; anticorrosive

Citation: Rao, Q.; Weng, L.; Zhang, J.; Chen, Y.; Yang, Y.; Liu, D.; Duan, Y.; Cao, Y.; Chen, J.; Li, X.; et al. A Titanium-Based Superhydrophobic Coating with Enhanced Antibacterial, Anticoagulant, and Anticorrosive Properties for Dental Applications. *Coatings* **2024**, *14*, 571. https://doi.org/10.3390/coatings14050571

Academic Editor: Kirill A. Emelyanenko

Received: 27 March 2024
Revised: 22 April 2024
Accepted: 1 May 2024
Published: 5 May 2024

1. Introduction

Titanium (Ti) and its alloys are extensively utilized as dental implantable materials, such as dental implants, orthodontic brackets, orthodontic arch wires, and removable partial denture connectors because of their great biocompatibility and sufficient biomechanical properties [1,2]. Nanostructuring titanium [3] makes it possible to improve the mechanical properties and reduce the size of implants. However, mechanical behavior similar to bone tissue is achieved only in near-beta Ti alloys due to titanium alloying [4]. The surface acquires biocompatible properties when forming dense coatings, for example, from titanium dioxide (TiO_2) [5], which not only prevents the release of metal ions into a living organism but also improves the spread and growth of living cells, as well as tribological properties. In recent decades, Ti and other kinds of metal implants have benefited millions of patients, including the elderly, athletes, and victims of car accidents, to functionally heal their damaged tissues and enhance their life quality [1,6]. However, a significant drawback of the implants is the potential for infection-related failure, which frequently

results in severe damage and may necessitate additional surgeries, substantial economic costs or even death [7–9]. It has been stated that bacterial infections have caused failure in 1.5% of orthopedic implants in Europe and 8% of cardiovascular implants in the United States [10]. For dental implants, the primary cause of implantation failure is peri-implant inflammatory illnesses like peri-implantitis, which can generally lead to peripheral bone loss and may limit the service life of the implant [11,12]. Typically, implant infections are highly complicated, multifactorial, and challenging to cure [12]. The most common bacteria related to implant infections are Gram-positive bacteria like *Staphylococcus aureus* (*S. aureus*) and Gram-negative bacteria such as *Porphyromonas gingivalis* (*P. gingivalis*, *P.g*) [13]. Also, they may cause blood-contacting issues, i.e., the interplay between metal implants and blood components might result in unfavorable clinical outcomes such as hemolysis, infections, and thrombosis [14]. Specifically, the occurrence of thrombus and infections continues to be a major obstacle to the effectiveness of blood-contact implants because of the adherence of bacteria and platelets during long-term usage [15]. This may prevent blood flow at the implant site and cause ischemia, infarction, and ultimately death [16]. Furthermore, Ti-based metals interact with saliva or body fluids after being implanted in human tissues, and corrosion occurs slowly as a result of complicated electro-biochemical reactions at the implant–tissue interfaces [17], which contributes to infection and the failure of implants as medical devices. Both the release of large amounts of metal ions and the acidic environment due to the presence of a large number of bacteria tend to accelerate the corrosion of metal implants [18,19]. Thus, to increase the use of Ti-based implants in dental applications, a Ti-based superhydrophobic coating with enhanced antibacterial, anticoagulant, and anticorrosive properties has been proposed.

Superhydrophobic surfaces with a water contact angle (WCA) greater than 150° and a sliding angle (WSA) smaller than 10° have sparked considerable attention in both academic studies and practical applications due to their distinctive abilities, such as water resistance [20,21], self-cleaning [22], anticorrosion [23], anti-icing [24,25], and oil–water separation [26]. In recent years, a wide range of approaches for creating superhydrophobic coatings have been reported, including sol–gel [27,28], chemical etching [29], laser fabrication [30], hydrothermal reactions [31,32], electrospinning [33], plasma spraying [34], and anodization [35,36]. For instance, Souza et al. [37] created a new superhydrophobic coating on the titanium surface by using a one-step glow discharge plasma method to significantly lower polymicrobial attachment and biofilm formation on biomedical implants. Additionally, the results of the corrosion tests showed that the superhydrophobic coating displayed a larger diameter on the Nyquist plot, a higher impedance, a bigger phase angle at high frequency, a lower corrosion current density, and a higher corrosion potential in artificial saliva as compared to Ti samples, which reveals that the superhydrophobic surface has improved corrosion resistance. Tang et al. [38] fabricated superhydrophobic nanotube-structured TiO_2 films via the electrochemical oxidation and self-assembly of 1H,1H,2H,2H-perfluorooctyltriethoxysilane (PTES), which can prevent *S. aureus* attachment successfully and could be utilized in orthopedic applications. Bartlet et al. [39] fabricated a superhydrophobic Ti-based coating surface through anodization, chemical etching, and surface silanization with (heptadecafluoro-1,1,2,2-tetrahydrodecyl)trichlorosilane, which could effectively prevent the long-term development and biofilm formation of *S. aureus* and *Pseudomonas aeruginosa* (*P. aeruginosa*) on implantable biomedical devices like pacemakers and artificial heart apparatus. Montgomerie et al. [40] produced superhydrophobic coatings to create TiO_2 nanoflowers by employing the hydrothermal method and gas-phase silanization process with PTES, which is of significant benefit in preventing the adherence of *S. aureus* (Gram-positive bacteria) and *E. coli* (Gram-negative bacteria) as well as biofilm formation. It is expected to be applied in blood-contact devices, including heart valves and stents. Zhang et al. [41] created controlled superhydrophobic coatings on pure Ti surfaces by sequentially applying an ultraviolet laser process, ultrasonic acid treatment, and PTES modification, which is efficient in preventing the adherence of blood cells and thrombosis, and enhancing corrosion resistance on Ti substrates. Yang et al. [42] constructed a superhy-

drophobic surface on Nitinol Shape Memory Alloy (NiTi SMA) with a WCA of 155.4° and a WSA of 4.4° by the combination of laser treatment and polydimethylsiloxane (PDMS) modification. The as-fabricated superhydrophobic coating exhibited superior corrosion resistance in the simulated body fluid (SBF) solution as compared to an untreated NiTi alloy and a NiTi alloy purely ablated by a nanosecond laser, indicating its potential application in the medical field. However, some of the techniques are inappropriate for large-scale applications because of the complex equipment used, high costs, mechanical restrictions, etc. [27]. In comparison, anodization is the process that is the most frequently utilized because it is simple to create an organized structure of nanotube oxides on Ti-based implants [43,44]. For the surface modification, it is noted that there are stricter regulations enforced by the global regulatory bodies on the use of fluoro- or perfluoro compounds. However, fluorosilanes have been reported for use in medical applications such as dental, orthopedic, and cardiovascular implants [38–41], especially for 1H,1H,2H,2H-perfluorodecyltriethoxysilane (FAS), showing no cytotoxicity. FAS was chosen due to its chemical stability and its ability to interact with the surface under mild conditions [45], and thus can be widely used to obtain superhydrophobicity on metal, paper, glass, and ceramic substrates and silica membranes, and the FAS-based coating has a long chain of fluorocarbons that can repel both water and oil [46]. Furthermore, it has the ability to quickly form self-assembled monolayers when hydrophilic surfaces are functionalized [47]. The superhydrophobic surfaces work through the combination of a rough structure with low-surface-energy material modification to produce the Cassie–Baxter state, providing an entrapped air layer to obtain a large WCA [48] and drastically restricting the interplay between microorganisms or blood cells and the coating surface. However, there are few reports related to superhydrophobic Ti-based coatings that endow materials with good antibacterial, anticoagulant, and anticorrosive properties simultaneously in dental applications.

In this study, we prepared a superhydrophobic coating on the Ti surface through the synergistic effect of anodization to create a rough structure and carried out surface modification with FAS to lower the surface energy. The adhesion of *S. aureus* and *P.g* on the as-prepared Ti-based superhydrophobic coating was evaluated, demonstrating that less *S. aureus* and *P.g* can be attached to it as compared to the bare Ti after culture for 4, 12, and 24 h. In addition, the biocompatible, anticoagulant, and anticorrosive properties and biosafety were also examined.

2. Materials and Methods

The Ti foils (purity: 99.9%, thickness: 0.1 mm), Ti wires (diameter: 0.1 mm), and Ti rods (diameter: 3 mm, length: 7 mm) were obtained from Rongbiao Metal Materials Co., Ltd., Xingtai, China. 1H,1H,2H,2H-perfluorodecyltriethoxysilane (FAS, $(OC_2H_5)_3Si(CH_2)_2(CF_2)_7CF_3$; purity: 97%), ethylene glycol, and ammonium fluoride (NH_4F) were supplied by Aladdin Bio-Chem Technology Co., Ltd., Shanghai, China. Anhydrous ethanol was provided by Bohuatong Chemicals Sales Centre, Tianjin, China. All reagents were analytical-grade and utilized without any additional processing. *S. aureus*, *P.g*, and the mouse fibroblast cell line L929 were acquired from Key Lab. of Oral Diseases Research at Anhui Medical University (AHMU), Hefei, China.

2.1. Sample Preparation

The Ti foils were cut into pieces with a size of 10 cm × 5 cm. Ti wires (for the abdominal aortic implantation *in vivo* experiment) and Ti rods (for the subcutaneous implantation *in vivo* experiment) were ultrasonically washed with anhydrous ethanol and deionized (DI) water sequentially to eliminate dust and other pollutants. The cleaned Ti foil was anodized in a glycol solution electrolyte with 0.25 wt.% ammonium fluoride and 2.0 wt.% DI water at continuous voltages ranging from 15 V to 55 V for 1 h at room temperature. Then, the anodized Ti foils were washed with DI water and dried further. Subsequently, these as-fabricated specimens were ultrasonically modified in an ethanol solution containing 1.0 wt.% FAS for 0.5 h and heated in an oven at 100 °C for 1 h. The anode and cathodes were Ti

foil and a graphite plate, with a distance of 4 cm. A simplified diagram of the preparation process is displayed in Figure 1. Ti, AO, Ti + FAS, and SH represent bare Ti, anodized Ti, Ti modified by FAS, and Ti-based superhydrophobic coating produced via anodization followed by FAS modification, respectively.

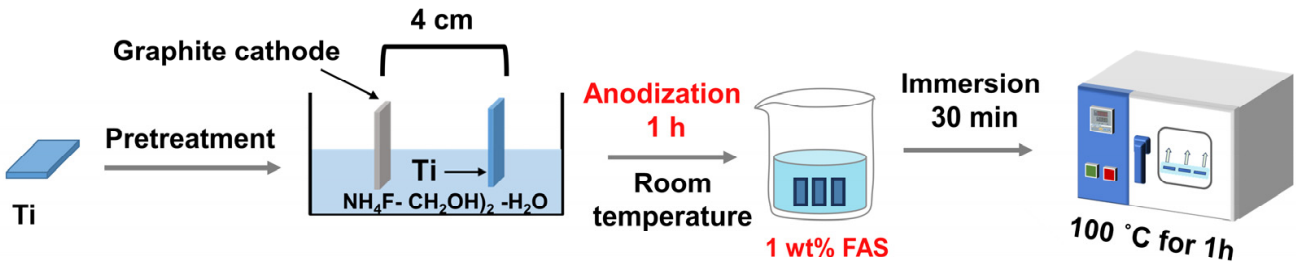

Figure 1. A simplified diagram of the preparation process.

2.2. Characterization of Ti-Based Superhydrophobic Coating

2.2.1. Surface Wettability

The WCA, WSA, water contact angle hysteresis, and surface energy were obtained via a contact angle measurement device (OCA 15EC, DataPhysics Corporation, Filderstadt, Germany) at three points on every specimen (n = 5 per group) with 5 µL DI water droplets at room temperature.

2.2.2. Surface Morphology, Roughness, and Chemical Composition

The surface morphology and elemental composition were characterized by a scanning electron microscope (SEM, ZEISS GeminiSEM 300, Carl Zeiss, Baden-Wurttemberg, Germany) with an attached energy-dispersive X-ray spectrometer (EDS). The surface roughness with a scanning area of 20 mm × 20 mm was investigated by an atomic force microscope (AFM, NanoWizard 4XP, Bruker, Gernsheim, Germany). The surface composition and crystal structures were examined by a Fourier transform infrared (FTIR, Thermo Scientific Nicolet iS20, Thermo Scientific, Waltham, MA, USA) spectrometer, X-ray photoelectron spectroscopy (XPS, Thermo Scientific K-Alpha, Thermo Scientific), and X-ray diffractometer (XRD, BrukerAXS D8, Bruker, Berlin, Germany).

2.3. Biocompatibility Test

The L929 cell was used to evaluate biocompatibility. To gather extract liquids, the sterilized samples were first immersed in a MEM medium (PM150410, ProCell, Wuhan, China) containing 10 vol.% fetal bovine serum (FBS, Wisent, Nanjing, China) and 1 vol.% penicillin–streptomycin (Beyotime Biotechnology, Shanghai, China) for 3 days. The L929 cells were pre-seeded in cell slides at the bottom of a 12-well plate with a density of 10^4 cells per well and then co-cultured with various extract liquids. The L929 cell slides cultured with MEM medium containing 10 vol.% FBS and 1 vol.% penicillin–streptomycin were used as the control group. After incubation for 1, 3, and 5 days, the viability of the L929 cell was measured via the Cell Counting Kit-8 approach (CCK-8, Biosharp, Beijing, China). The value of OD_{450} was measured after incubation for 3 h to obtain the cell viability calculated by the following Equation (1):

$$Cell\ viability = \frac{A - B}{C - B} \times 100\% \quad (1)$$

where A, B, and C represent the OD value of the experimental sample (extract liquids of Ti, AO-35 V, Ti + FAS, and SH-35 V groups), a blank sample (90 vol.% MEM medium and 10 vol.% CCK-8 solution), and the control sample, respectively. Subsequently, all samples were fixed with 2.5 vol.% glutaraldehyde overnight, stained for 10 to 15 min with rhodamine 123 (Biodee, Beijing, China), and evaluated via a fluorescence microscope.

2.4. Antibacterial Test

The major infectious bacterium associated with metal implants, *S. aureus*, was chosen for the subsequent bacterial examination [49]. Meanwhile, *P.g*, a Gram-negative anaerobic bacterium indicated as a significant pathogen linked with peri-implantitis and periodontitis [50,51], was employed in this study to test the antibacterial activity. Before diluting to a concentration of 10^6 CFU/mL for the antibacterial experiment, *S. aureus* was incubated in a brain heart infusion broth (BHI, Hopebio, Qingdao, China) for 12 h, while *P.g* was incubated anaerobically in BHI broth containing vitamin K, hemin, and L-cysteine hydrochloride (both from Hopebio, Qingdao, China) for 48 h. Each sample was divided into small pieces with a size of 1 cm × 1 cm and sterilized for 1 h via ultraviolet (UV) light before the antibacterial test.

After sterilization, each sample was added to 24-well plates along with 1 mL of the bacterial suspension per well. All samples were rinsed once with phosphate-buffered solution (PBS) to remove the planktonic bacteria after cultivation at 37 °C for 4 h, 12 h, and 24 h. These samples were randomly divided into three groups. The adherent *S. aureus* and *P.g* were collected from one group of samples by ultrasonic treatment in 1 mL BHI broth for 1 min. Then, the collected *S. aureus* was diluted 10^2, 10^3, and 10^4 times, respectively, and the adherent *P.g* was diluted 5, 10, and 10^2 times, respectively, and cultivated for 24 h and 15 days on BHI and blood agar plates to perform colony counting, respectively. Considering that the number of adhered bacteria on the sample surface increases with the extension of incubation time, a higher magnification of dilution is required for colony counting. The other group samples were fixed with 2.5 vol.% glutaraldehyde overnight, and then dehydrated with a gradient of 30 vol.%, 50 vol.%, 60 vol.%, 70 vol.%, 80 vol.%, 90 vol.%, 95 vol.%, and 100 vol.% ethanol for 10 min. Subsequently, these specimens were exposed to critical point drying equipment (Critical Point Dryer, K850, Quorum, England) and observed by SEM after gold spraying treatment (Ion Sputtering, 108Auto, Cressington, England). The remaining samples were exposed to rhodamine 123 for 10 min and observed by confocal laser scanning microscopy (CLSM, LSM880, Carl Zeiss, Baden-Wurttemberg, Germany).

The antibacterial rates (Ra) of adherent bacteria on each sample surface were calculated using the following Equation (2):

$$Ra = \frac{(C - E)}{C} \times 100\% \quad (2)$$

where C represents the average amount of adherent bacteria on the control group (bare Ti), and E indicates the average amount of adherent bacteria on the experimental group, involving Ti + FAS, AO-35 V, and SH-35 V.

2.5. In Vitro Hemolytic and Anticoagulant Tests

2.5.1. *In Vitro* Hemolysis Test

Fresh blood from the marginal ear vein of live New Zealand white rabbits was obtained and diluted with 0.9 wt.% NaCl solution at a volume ratio of 4:5. Ti, AO-35 V, Ti + FAS, and SH-35 V were placed in 0.9 wt.% NaCl of 9.8 mL in a water bath at 37 °C for 30 min, then 0.2 mL diluted blood was added with gentle shaking and incubation at 37 °C for 60 min. Then, 15 mL centrifuge tubes containing the samples were centrifuged at 3000 rpm for 5 min, and the supernatant was aspirated at 100 µL per well and placed in sterile 96-well plates [52]. The negative control group (hemolysis ratio: 0) was 0.9 wt.% NaCl of 9.8 mL with diluted blood of 0.2 mL, but the positive control group (hemolysis ratio: 100%) was DI water of 9.8 mL with diluted blood of 0.2 mL. The value of OD_{540} was measured to obtain the hemolysis ratio calculated by the following Equation (3):

$$Hemolysis\ ratio = \frac{(A - B)}{(C - B)} \times 100\% \quad (3)$$

where *A*, *B*, and *C* represent the OD value of the experimental group, the negative control group, and the positive control group, respectively.

2.5.2. *In Vitro* Static Test of Platelet Adhesion

Fresh blood from the marginal ear vein of live New Zealand white rabbits was centrifuged at 1500 r/min for 15 min, and the upper layer of platelet-rich plasma (PRP) was aspirated and placed in a 12-well plate. The sample surfaces were separately immersed in 500 μL of PRP per well and cultured in a water bath with a constant temperature of 37 °C for 45 min, and then gently cleaned with PBS 3 times until the unadhered platelets on the samples were cleaned. After fixation, dehydration, critical point drying, and gold spraying, the platelet adhesion on all samples was observed by SEM.

2.5.3. *In Vitro* Dynamic Test of Platelet Adhesion

Fresh whole blood was collected from healthy adult volunteers in this study and anticoagulated with sodium citrate at a volume ratio of 9:1 according to the ethics standards of Anhui Medical University. In a Chandler loop system, the samples were added to a polymer tube which was partially filled with whole blood to create a reclosable loop and rotated between 10 and 40 rpm in a temperature-controlled situation to mimic arterial bloodstream conditions. After circulation for 3 h, the blood was drained and the samples were gently cleaned with PBS 3 times until the unadhered blood was cleaned from the samples. After fixation, dehydration, critical point drying, and gold spraying, the platelet adhesion on each sample surface was observed by SEM.

2.6. Anticorrosive Test

The electrochemical corrosion examination was carried out via an electrochemical workstation (Versa STAT 3, AMETEK Corporation, Berwyn, PA, USA) utilizing a traditional three-electrode system with an exposed area of 1.0 cm^2 as the working electrode (WE), Ag/AgCl as the reference electrode (RE), and a platinum (Pt) sheet as the counter electrode (CE). The potentiodynamic polarization curves were examined after bare Ti and the Ti-based superhydrophobic coating were placed into the artificial saliva (pH = 7.0) for 0.5 h to obtain a steady open circuit potential (OCP). The WCA was then measured after placing them in ambient temperature for 12 h to dry completely. Meanwhile, their corresponding surface morphology was observed after the corrosion resistance test.

2.7. In Vivo Experiments

Six- or eight-week-old SD rats (about 150–200 g) were purchased from the Animal Experiment Center of Anhui Medical University. All animal experiments were performed following the guidelines of the Ethical Committee of Anhui Medical University. All rats were bred for one week and allocated to the bare Ti group or the Ti-based superhydrophobic coating group at random before the experiment.

2.7.1. Abdominal Aortic Implantation

Six- or eight-week-old SD rats were intraperitoneally anesthetized by injecting 3 wt.% pentobarbital sodium (0.15 mL/100 g weight). After shaving and disinfecting with iodine, abdominal skin and musculature were incised sequentially and the viscera were moved to one side to expose the abdominal aorta. The abdominal aorta and vein were then separated and the aorta was clamped with vascular clips, and, eventually, bare Ti wire and superhydrophobic Ti wire were implanted, respectively. After implantation for 1 h, all samples were removed and then fixed in 2.5 vol.% glutaraldehyde overnight, dehydrated by an alcohol gradient, sprayed with gold, and observed by SEM.

2.7.2. Subcutaneous Implantation

The bare Ti rod and the superhydrophobic Ti rod were applied to assess the biosafety of the surrounding tissues in the six-week-old SD rats. These rats were anesthetized by

intraperitoneally injecting 3 wt.% pentobarbital sodium before the operation, and then the hairs on the back were shaved and disinfected with iodine. Subsequently, a longitudinal incision of 10 mm was cut on each side of the back and bluntly peeled with scissors to create a pocket into which the Ti rod and superhydrophobic Ti rod were implanted, and finally sutured. After 7, 15, and 28 days, the rats were euthanized, and all implanted samples with the local soft tissues were collected for subsequent histological examination, involving hematoxylin and eosin (HE) staining and Masson staining.

2.8. Statistical Analysis

All data are shown as mean ± standard deviation (SD) and were analyzed by GraphPad Prism version 9.0 (GraphPad Software, Boston, MA, USA) via one-way or two-way analysis of variance (ANOVA). All tests were performed three or more times and the statistical significance was given as $p < 0.05$ (*), $p < 0.01$ (**), and $p < 0.001$ (***).

3. Results and Discussion

3.1. Characterization of Ti-Based Superhydrophobic Coating

3.1.1. Surface Wettability

To assess the hydrophobicity, both WCA and WSA were measured according to the change in anodization voltages for different samples. As demonstrated in Figure 2 and Table 1, the bare Ti has a WCA of 83.8 ± 3.3°, indicating its hydrophilic nature. However, the WCA was decreased to 23.2 ± 3.3° after anodization at 35 V, showing a more hydrophilic state. Meanwhile after modification by FAS alone, Ti + FAS had a WCA of 115.4 ± 3.2°, which made it hydrophobic. After anodization and FAS modification together, the WCA generally exhibited an increasing and then decreasing trend. When the voltage reached up to 35 V, the coating had the highest WCA of 159.9 ± 5.8° and the lowest WSA of 2.7 ± 2.2° among all samples. However, the WCA had an obvious decline without reaching superhydrophobicity when the voltage was more than 40 V. It is evident that the SH-35 V was the optimal coating for all the prepared samples. As demonstrated in Table 1, the water contact angle hysteresis (0.9 ± 0.5°) and the surface energy (1.9 ± 0.3 mN/m) of SH-35 V were the lowest among all samples, which is generally in accordance with the trend of WCA and WSA. The apparent contact angle on a heterogeneous surface can be characterized by the Cassie–Baxter equation, Equation (4):

$$\cos\theta^* = f_1\cos\theta_1 + f_2\cos\theta_2 \quad (4)$$

where f_1 and f_2 are the surface area fractions of substances 1 and 2 ($f_1 + f_2 = 1$). θ_1 and θ_2 are the intrinsic contact angles on two different substances. θ^* is the apparent contact angle on the sample surfaces. If the surface is superhydrophobic, which means it can preserve air, substance 2 represents the entrapped air, and $\theta_2 = 180°$. Equation (4) can be simplified as

$$f_2 = f_1\cos\theta_1 - \cos\theta^* \quad (5)$$

As the surface area fraction of trapped air increases, the apparent contact angle can improve. Based on the WCA of the Ti + FAS and the SH-35 V surfaces, it can be calculated that f_1 is 0.107, i.e., when a water droplet is in contact with the SH-35 V surface, the contact area between the water droplet and the solid surface is only 10.7% while the contact area between the water droplet and the air is the largest at 89.3%. This suggests that the synergistic effect of rough structure and low surface energy modification is the key to fabricating superhydrophobic surfaces.

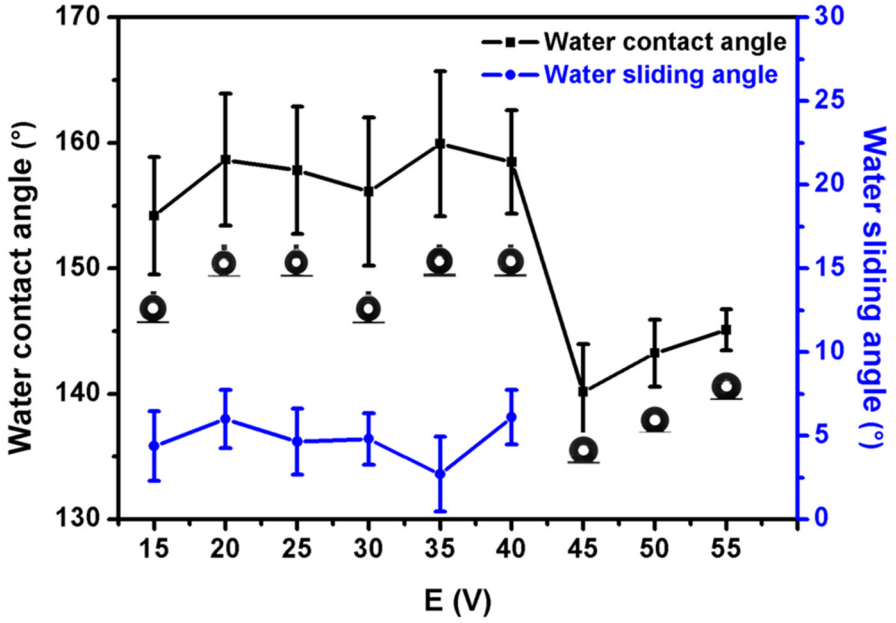

Figure 2. WCA and WSA of coatings via anodization with different voltages for 1 h followed by FAS modification.

Table 1. WCA, WSA, water contact angle hysteresis, surface energy, and f_2 of different samples.

Samples	Water Contact Angle (°)	Water Sliding Angle (°)	Water Contact Angle Hysteresis (°)	Surface Energy (mN/m)	f_2
Ti	83.8 ± 3.3	-	-	31.8 ± 3.3	-
AO-35 V	23.2 ± 3.3	-	-	52.7 ± 6.3	-
Ti + FAS	115.4 ± 3.2	-	-	12.1 ± 2.2	-
SH-15 V	154.2 ± 4.7	4.4 ± 2.1	1.5 ± 0.5	2.4 ± 1.0	0.825
SH-20 V	158.7 ± 5.3	6.0 ± 1.7	1.7 ± 1.2	2.0 ± 0.7	0.881
SH-25 V	157.8 ± 5.1	4.7 ± 2.0	2.5 ± 1.5	2.2 ± 1.0	0.870
SH-30 V	156.1 ± 5.9	4.8 ± 1.5	1.6 ± 1.8	2.0 ± 0.5	0.849
SH-35 V	159.9 ± 5.8	2.7 ± 2.2	0.9 ± 0.5	1.9 ± 0.3	0.893
SH-40 V	158.5 ± 4.1	6.1 ± 1.6	1.6 ± 1.8	1.9 ± 0.7	0.877
SH-45 V	140.2 ± 3.8	-	-	4.6 ± 2.3	0.594
SH-50 V	143.2 ± 2.7	-	-	2.4 ± 0.9	0.651
SH-55 V	145.1 ± 1.6	-	-	1.9 ± 0.5	0.685

The dynamic behavior of water droplets on different sample surfaces is shown in Figure S1. The bare Ti and SH-35 V were placed horizontally and in contact with a 5 µL water droplet. It is obvious that the water droplet attaches to the bare Ti surface and gradually spreads out [Figure S1(a_2–a_5)], demonstrating its hydrophilicity (Video S1). In contrast, the shape of the water droplet changes when it comes into contact with the SH-35 V surface [Figure S1(b_2)] and deforms as the contact area between the water droplet and the sample surface increases throughout the compression process [Figure S1(b_3)]. Surprisingly, the water droplet retracts from the surface [Figure S1(b_4)] and returns to its previous spherical shape [Figure S1(b_5)] once the needle tip is elevated. During the compression and elevation process, the SH-35 V surface remains unwetted, which indicates that SH-35 V has low adhesion with water and effectively prevents surface wetting (Video S2).

To visualize the water repellency for the SH-35 V surface, the water flow continuously impinges on the sample surface to observe the dynamic moving process, as shown in Video S3. It can be clearly observed that the reflected water jet flow can easily bounce off without leaving any traces due to the superhydrophobic nature of SH-35 V. To further examine the interaction between the water and the sample surface, the SH-35 V exhibited

a mirror-like phenomenon (Video S4) when immersed in water. The mirror effect can be observed with a certain glancing angle due to the luminous reflectivity at the entrapped air layer on such surfaces.

In consideration of its dental application, artificial saliva was also applied to evaluate the CA. As shown in Figure S2, SHs show high hydrophobicity, with the highest CA of 159.4° on SH-35 V. Moreover, the wettability of different kinds of liquids (10 μL) on SH-35 V was also evaluated. As shown in Figure S3, the CAs are greater than 130°, demonstrating its high hydrophobicity for the common liquids.

In addition, we evaluated the life of the superhydrophobic coating by examining CA over time. As shown in Figures S4 and S5, the CAs of water and artificial saliva on SH-35 V were 159.2 ± 2.2° and 157.6 ± 0.7° after storing at ambient temperature in air for 730 days, respectively. Both of them are greater than 150°, so they can still maintain their superhydrophobic performance. Further, after immersion in artificial saliva for 2 days, the CAs of water and artificial saliva on SH-35 V were 132.8 ± 1.1° and 133.6 ± 1.7°, respectively, indicating its high hydrophobicity, although it lost its superhydrophobicity, and indirectly demonstrating that the leaching of these FAS compounds is limited in artificial saliva over time (Figures S6 and S7). Therefore, it can be concluded that the superhydrophobicity is the result of the synergistic effect of anodization to construct the rough structure and hydrophobic modifications to lower the surface energy, and an ideal anodization voltage to fabricate the Ti-based superhydrophobic coating is 35 V.

3.1.2. Adhesion Test of AO

According to ASTM D3359, a hundred-grid cutter is suitable for the evaluation of the coating adhesion. The adhesion between the coating and the substrate was classified as 5B, 4B, 3B, 2B, 1B, and 0B, of which 5B indicates that there is no detachment on all grids and the coating adhesion is the strongest, and 0B means that the detachment area of the grid is more than 65% and the adhesion between the coating and the substrate is the worst. A small amount of detachment can be observed on the AO-15 V surface and does not exceed 5% of the grid area, which was graded as 4B [Figure 3a]. As shown in Figure 3b–f, the AO surfaces with anodization voltages from 20 V to 40 V showed almost no detachment and the cross-cut pattern remained intact, which was rated as 5B. However, the AO surfaces with anodization voltages of 45–55 V were obviously detached, where the detachment area of AO-55 V was greater than 5% but less than 15%, and classified as 3B, as shown in Figure 3g–i. Thus, the adhesion between the coating and the substrate is gradually weakened when the anodization voltages are greater than 40 V.

3.1.3. Surface Morphology and Chemical Composition

The surface morphology of different samples is shown in Figure 4. The bare Ti surface is relatively smooth with some sanding scratches, as shown in Figure 4(a_1,a_2). The closely arranged nanopores were formed on AO-35 V after anodization, as seen in Figure 4(b_1,b_2). However, after modification by FAS alone, Ti + FAS surface covered by an FAS-modified layer becomes smoother, as observed in Figure 4(c_1,c_2). SH-35 V was entirely covered by a rough structure with the nanopores, as shown in Figure 4(b_2,d_2). It is noticeable that there is no difference in the surface structure changes between the anodized and superhydrophobic surfaces, indicating that the fluorination modification has almost no influence on the surface morphology. The WCA of SH-35 V was significantly larger than that of AO-35 V, which obviously indicates that the synergistic effect of both rough structure and low surface energy creates the superhydrophobic coating surface. Furthermore, the nanopore size of the TiO_2 nanotubes becomes gradually larger as the anodization voltage increases, as displayed in Figure S8. The SEM cross-sectional images of anodized samples at different voltages are shown in Figure S9. The length of the TiO_2 nanotubes, i.e., the thickness of the anodized samples, becomes longer from 500 nm to 4 μm as the anodizing voltage increases. Moreover, the anodized structures of Ti can still be maintained after

immersion in artificial saliva for 2 days, as shown in Figure S10, indicating the stability of anodized structures under such an environment.

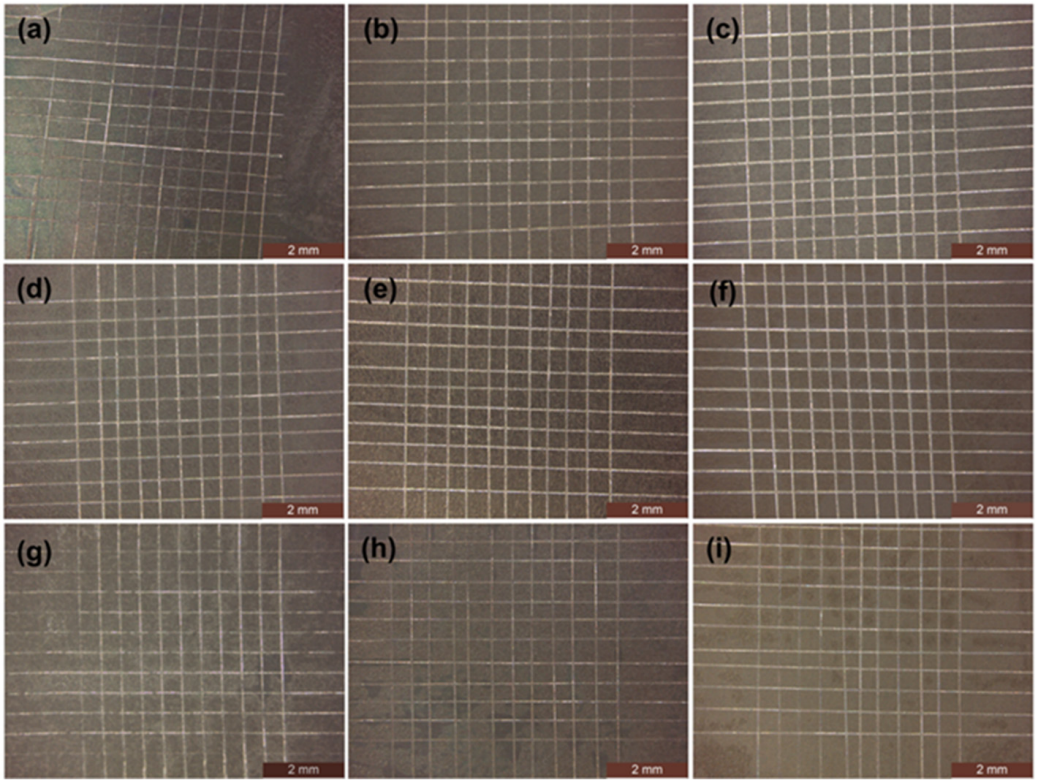

Figure 3. Images of adhesion test for AO: (**a**) AO-15 V, (**b**) AO-20 V, (**c**) AO-25 V, (**d**) AO-30 V, (**e**) AO-35 V, (**f**) AO-40 V, (**g**) AO-45 V, (**h**) AO-50 V, and (**i**) AO-55 V.

The EDS images of various samples are illustrated in Figure S11. As demonstrated in Figure S11a,b, the bare Ti surface consists of C and Ti while the AO-35 V surface is mainly composed of C, O, Ti, and F, which is from NH_4F of the electrolyte during anodization. In contrast, both F and Si appear on the Ti + FAS and SH-35 V surfaces, as illustrated in Figure S11c,d, which demonstrates that FAS was effectively self-assembled onto the two coatings surfaces [53]. As shown in Figure S11b–d, the weight percentage of F on SH-35 V is higher than AO-35 V and Ti + FAS, indicating that the amount of F is derived from both NH_4F and FAS.

Figure 5 demonstrates the AFM images of Ti, AO-35 V, Ti + FAS, and SH-35V, whose root-mean-square roughness (Rq) were 34.31 nm, 169.6 nm, 27.41 nm, and 120.4 nm, respectively. As demonstrated in Figure 5b, the AO-35 V surface is sufficiently rough, but it lacks FAS modification, exhibiting more hydrophilicity. In such a state, capillarity occurs, which can result in water droplets filling in the porous structure on the rough hydrophilic surface. As shown in Figure 5c, the roughness of Ti + FAS decreased slightly due to the low-surface-energy layer of FAS assembled onto the Ti surface. However, it was too flat to create a superhydrophobic surface, only exhibiting a certain degree of hydrophobicity. When compared to Figure 5b, the surface roughness of SH-35 V (Figure 5d) decreased, indicating that FAS may have partially filled the TiO_2 nanotubes. It can be found from the above-mentioned results that the surface with the greatest roughness did not show the biggest CA, indicating that although the roughness is essential for producing a superhydrophobic surface, it is not simply associated with the roughness alone. That is to say, the CA of the sample is influenced by both surface chemistry and intricate rough structures.

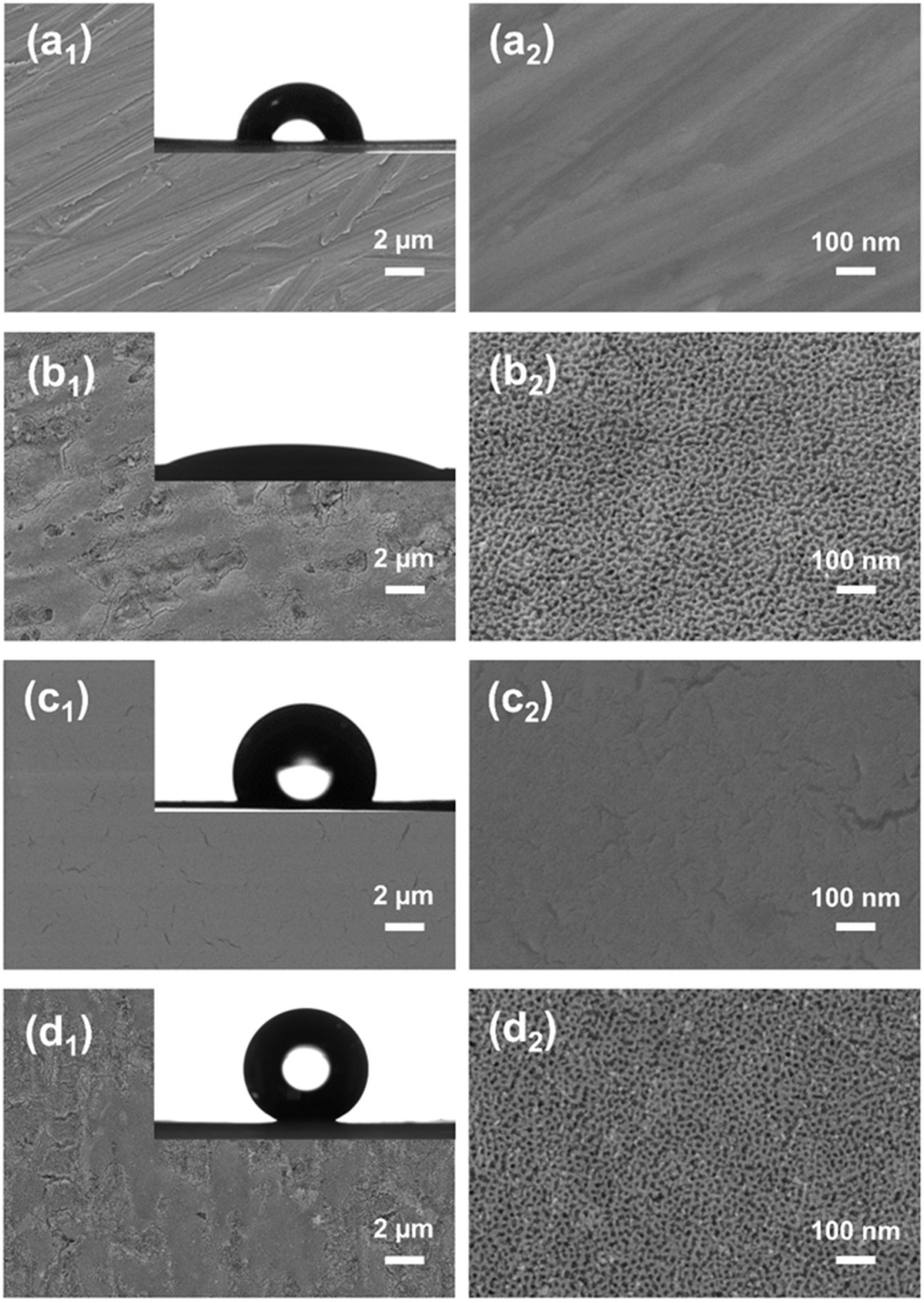

Figure 4. SEM images of different samples: (**a**$_1$,**a**$_2$) Ti, (**b**$_1$,**b**$_2$) AO-35 V, (**c**$_1$,**c**$_2$) Ti + FAS, and (**d**$_1$,**d**$_2$) SH-35 V.

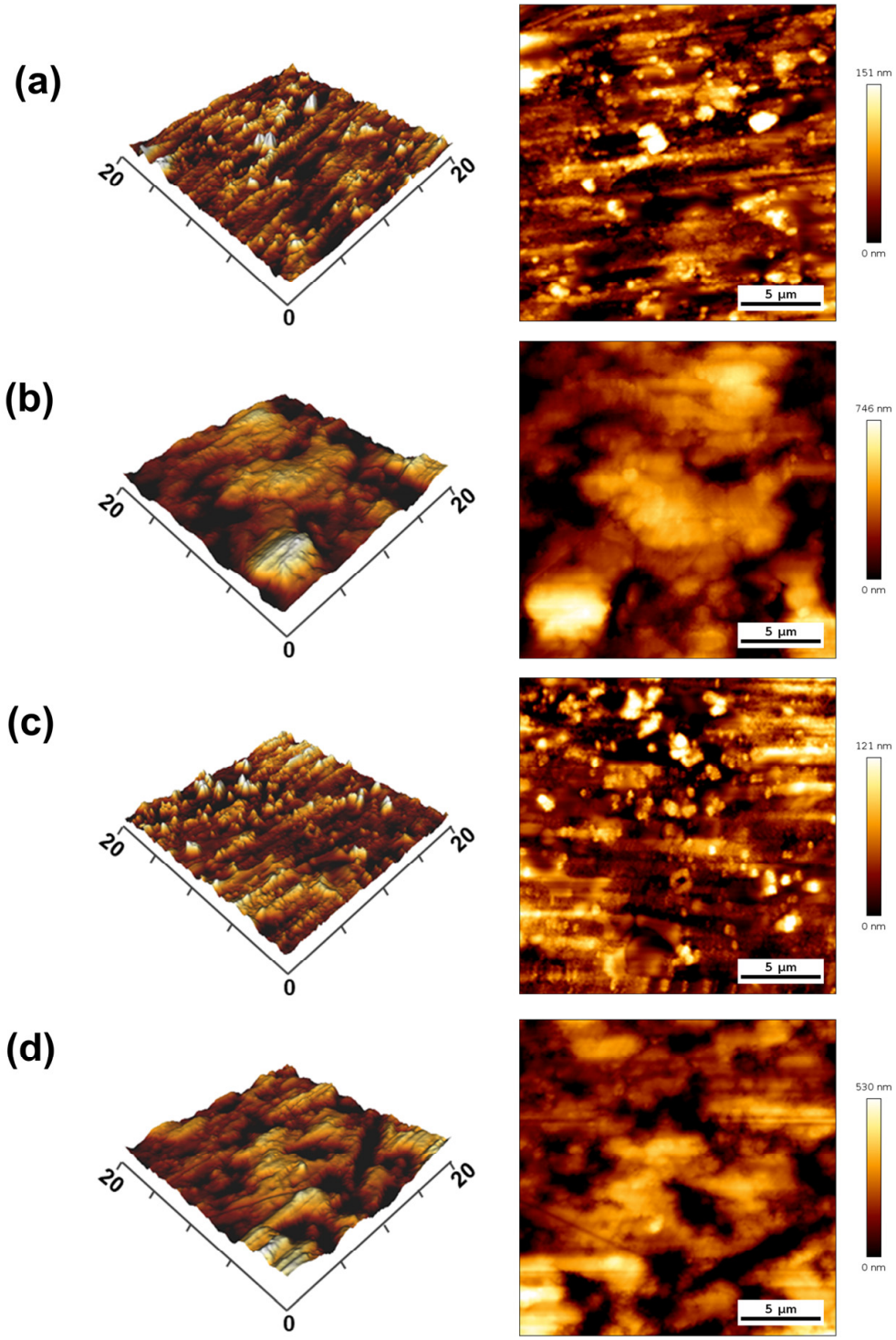

Figure 5. AFM images of different samples: (**a**) bare Ti, (**b**) AO-35 V, (**c**) Ti + FAS, and (**d**) SH-35 V.

The FTIR images of various samples are displayed in Figure 6a. The wide peak at 3324 cm^{-1} was produced by the tensile vibration of the −OH group. Antisymmetric tensile vibration peaks of the $-CH_3$ and $-CH_2-$ groups are characteristically observed at 2881 cm^{-1} and 2973 cm^{-1}, and Si−O bonds could be detected at 1086 cm^{-1}, 1042 cm^{-1}, and 867 cm^{-1} in the FAS solution [54]. For FAS, the typical peaks between 1200 cm^{-1} and 1350 cm^{-1}, which relate to the vibrations of the $-CF_3$ and $-CF_2-$ groups, serve as an indicator of organic fluorine concentrations [55]. After anodization at 35 V, Figure 6a exhibits distinctive bands at 3500–3200 cm^{-1} and 1640–1630 cm^{-1}, which are related to tensile vi-

bration of the −OH group and deformation of the −OH group of Ti−OH, respectively [56]. The vibration of the Ti−OH and Ti−O bonds corresponded to 1065 cm^{-1} and 867 cm^{-1}, respectively, suggesting that TiO_2 was on AO-35 V and SH-35 V. Furthermore, after anodization and FAS modification together, a distinct Si−O−Si peak at about 1153 cm^{-1} occurred on SH-35 V, indicating that FAS was effectively self-assembled onto AO-35 V; in other words, a superhydrophobic coating was fabricated. The reaction mechanism is explained in Figure 6b. The FAS is composed of a long hydrophobic chain of $-(CH_2)_2(CF_2)_7CF_3$ and $-Si(OC_2H_5)_3$, which first undergo hydrolysis to generate silanols (Si−OH) as an extremely active intermediate. Then, the dehydration condensation reaction of the Si−OH group with the Ti−OH group on the Ti surface could produce a self-assembled monolayer, which would allow the FAS to be firmly self-assembled onto the Ti surface [57]. Additionally, a dehydration reaction between the Si−OH groups could also result in the formation of grafted polysiloxane. As a result, the long hydrophobic chain of $-(CH_2)_2(CF_2)_7CF_3$ at the end of the molecule can significantly lower the surface energy of the coatings.

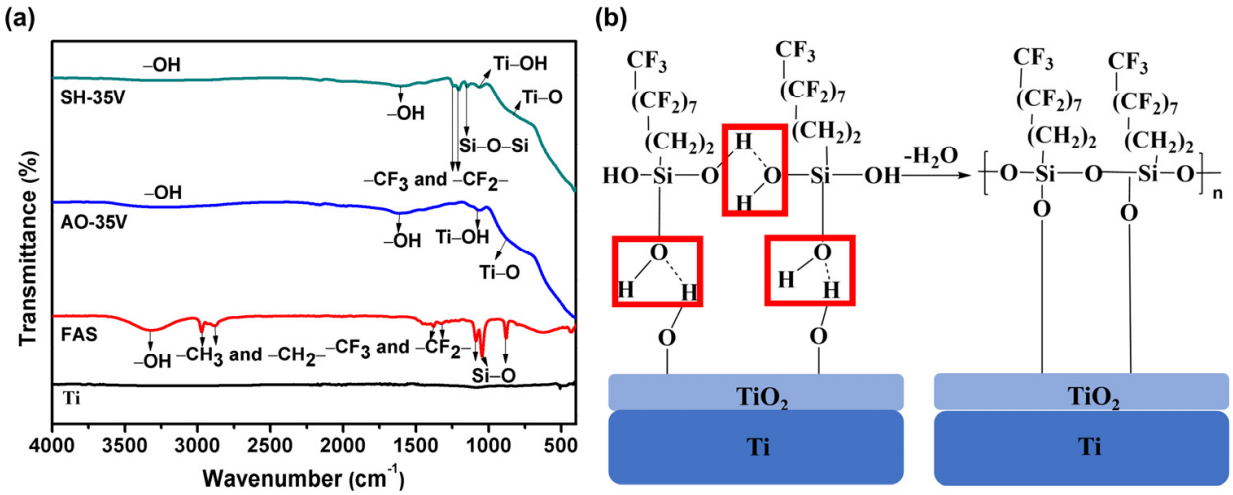

Figure 6. (**a**) FTIR images of Ti, FAS, AO-35 V, and SH-35 V samples, and (**b**) the dehydration condensation reaction of FAS on the Ti-based superhydrophobic coating surface.

XPS spectra were utilized to further identify the chemical composition of the sample surfaces. AO-35 V displayed elements Ti, O, C and F, while SH-35 V demonstrated the existence of elements Ti, O, C, F, and Si, as shown in Figure 7a. The existence of a strong F 1s peak, the presence of a Si 2p peak, and the decrease in Ti 2p and Ti 2s peaks indicate that FAS was effectively anchored on the AO-35V surface (Figure 7a). Figure 7b exhibits a higher C−H peak at 284.8 eV, which diminished and $-CF_3$ and $-CF_2-$ emerged after anodization and FAS modification, illustrating the AO-35 V surface was covered by FAS. As shown in Figure 7c, there is a substantial rise in the F 1s intensity at 688.5 eV, which is attributed to the FAS monolayer, and the sudden reduction in the F 1s at 684.4 eV, which is ascribed to the absorption of anions by a thin oxide film in the fluoride-containing electrolyte during the anodization [58]. It is clear from the present work that the chemical composition can play an important role in surface wettability. The crystal structures of AO-35 V and SH-35 V were investigated by XRD. As demonstrated in Figure S12, both of the coatings showed the same phase compositions of Ti and anatase, suggesting that the silanization treatment has almost no impact on the underlying crystal structure [39,59].

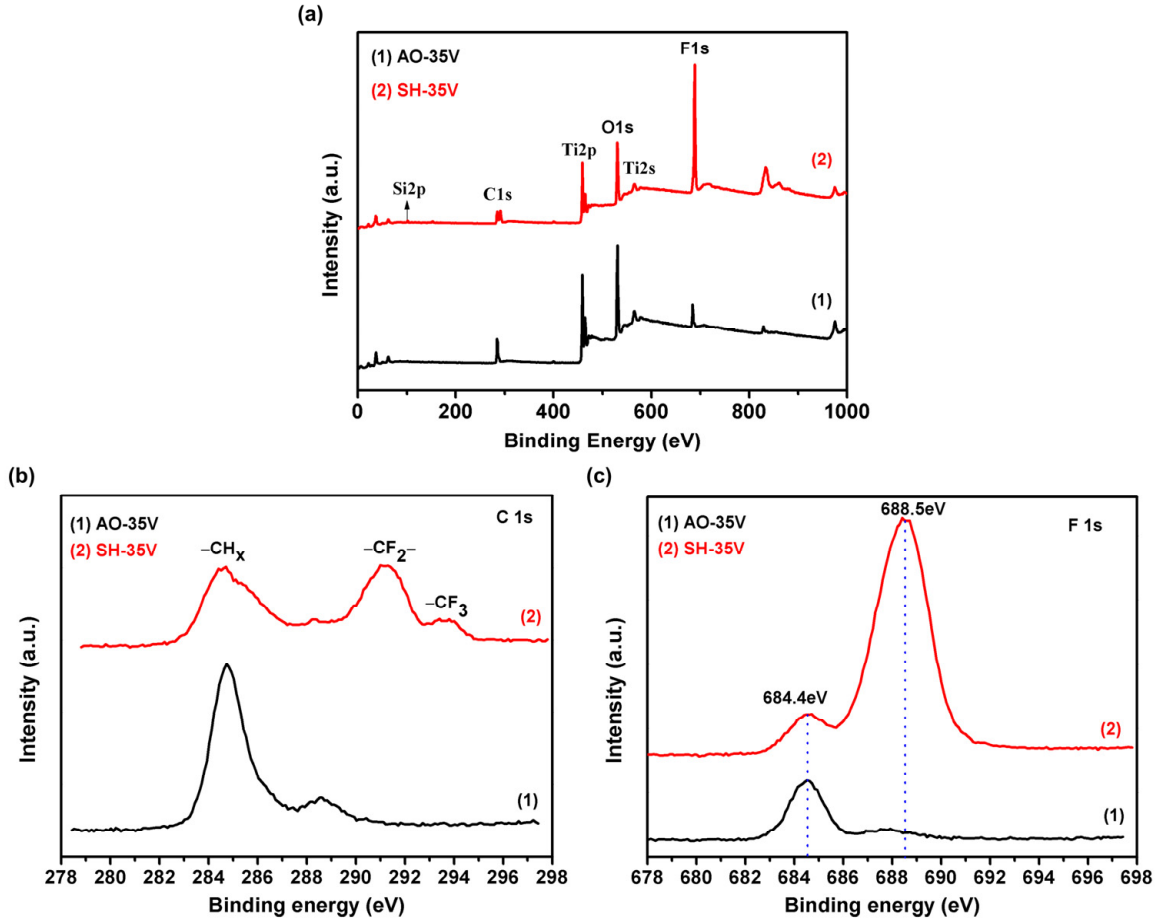

Figure 7. (**a**) XPS survey; high-resolution (**b**) C1s and (**c**) F1s spectra of AO-35 V and SH-35 V.

3.2. Biocompatibility Test In Vitro

As is well known, good biocompatibility is the basis for the materials which are applied in the human body [60]. Therefore, the biocompatibility of Ti, AO-35 V, Ti + FAS, and SH-35 V was assessed by co-culturing L929 cells with the extract liquids of these samples. As shown in Figure 8A, the number of L929 cells gradually increased on all samples as the incubation time increased and there was no statistical significance in cell viability between the control and four experiment sample groups for 1, 3, and 5 days in the CCK-8 assay. The rhodamine 123 staining fluorescence photographs shown in Figure 8B revealed that the L929 cells could successfully adhere and grow on the cell slides of the control, Ti, AO-35 V, Ti + FAS, and SH-35 V groups and the number of L929 cells was gradually increased with the extension of the co-culture time. After co-culture for 1 day, the number of cells on the control, Ti, AO-35 V, and Ti + FAS groups was relatively larger than that on the SH-35 V group. However, it is worth noting that the SH-35 V group showed an increasing trend in the number of cells after 3 days, indicating its improved biocompatibility to some degree. After 5 days, the L929 cells could still successfully adhere to and spread on the cell slides of the experimental groups (Ti, AO-35 V, Ti + FAS, and SH-35 V), with approximately the same density as the control group. Moreover, the cell morphology on the AO-35 V, Ti + FAS, and SH-35 V groups was intact with apparent antennae, similar to the control and Ti groups. It can be concluded from the aforementioned results that the prepared superhydrophobic coating has good biocompatibility.

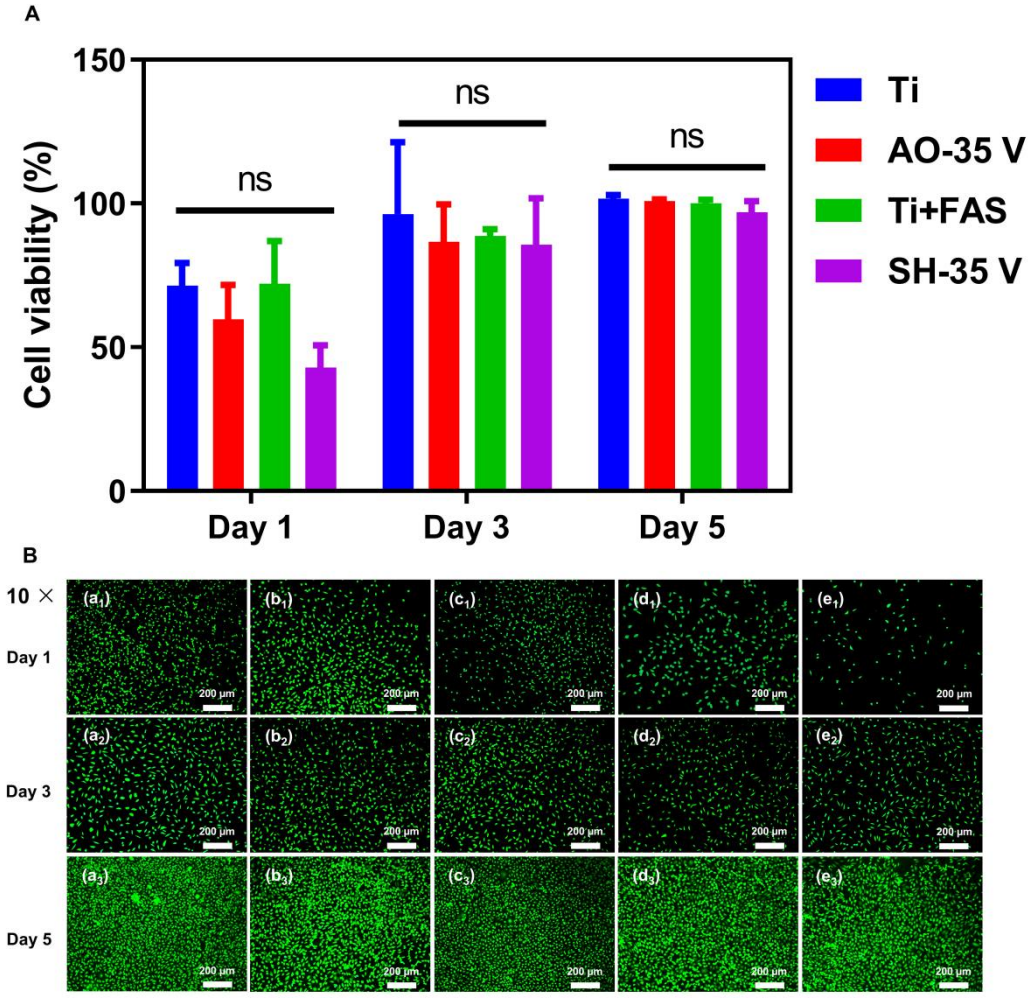

Figure 8. Biocompatibility evaluation of different samples: (**A**) Cell viability and (**B**) fluorescence microscope photographs of L929 cells co-cultured with extract liquids of different samples for 1, 3, and 5 days. (**a_1–a_3**) Control group, (**b_1–b_3**) bare Ti, (**c_1–c_3**) AO-35 V, (**d_1–d_3**) Ti + FAS, and (**e_1–e_3**) SH-35 V. All data are shown as mean ± standard deviation ($n \geq 3$) and analyzed by two-way ANOVA; ns represents no statistical significance ($p > 0.05$).

3.3. Antibacterial Test

The antibacterial results of various samples against *S. aureus* and *P.g* are exhibited in Figures 9 and 10, respectively. As indicated in Figure 9A,B and Figure 10A,B, AO-35 V showed the highest adhesion of *S. aureus* and *P.g* after cultivation for 12 h and 24 h because of the rough structure and the extremely high hydrophilicity [61]. In contrast, Ti + FAS exhibited relatively lower adhesion of *S. aureus* and *P.g* ($p < 0.05$). Amazingly, the number of *S. aureus* and *P.g* on SH-35 V was the lowest after cultivation from 4 h to 24 h among all samples, indicating its better antibacterial properties against *S. aureus* and *P.g*. It is mentioned that the number of bacteria gradually increased with the extension of incubation time, so the sample groups co-cultivated for 24 h need to be diluted by higher magnification to obtain countable plates. As a result, it seems that the number of colonies in the plate colony images of the 24 h sample groups is less than that of the 12 h sample groups for the antibacterial test against *S. aureus* (Figure 9A). Additionally, SEM was utilized to observe the morphology and the number of *S. aureus* and *P.g* on various samples. As observed in Figures 9C and 10C, spherical *S. aureus* and spherical and rod-shaped *P.g* adhered on all samples to different extents. There was a greater number of bacteria adhered on all samples after 24 h when compared to 4 h, which was anticipated because the longer incubation period gave the colonies of bacteria more time to grow and form [62,63]. As

seen in Figures 9C and 10C, a great number of colonies developed across the Ti and AO-35 V surfaces after 24 h, while only a small amount of *S. aureus* and *P.g* were scattered on the SH-35 V surface. The growth trend images of *S. aureus* and *P.g* obtained from CLSM were similar to those from SEM, as shown in Figures 9D and 10D. The above findings suggest that superhydrophobic surfaces can inhibit bacterial adhesion significantly, showing an excellent antibacterial property. This can be ascribed to the superhydrophobicity of the coating surface under the Cassie–Baxter state that could effectively inhibit bacteria from contacting with the sample surface [40]. The Cassie–Baxter state is contributed by the combination of rough TiO_2 nanotubes with modification of low-surface-energy substances to form high CA and an entrapped air layer, which can reduce the contact area between the bacteria and the coating surface to prevent bacterial adhesion on the surface from the start, thus decreasing the incidence of caries, peri-implantitis, mucositis, and surgical site infections.

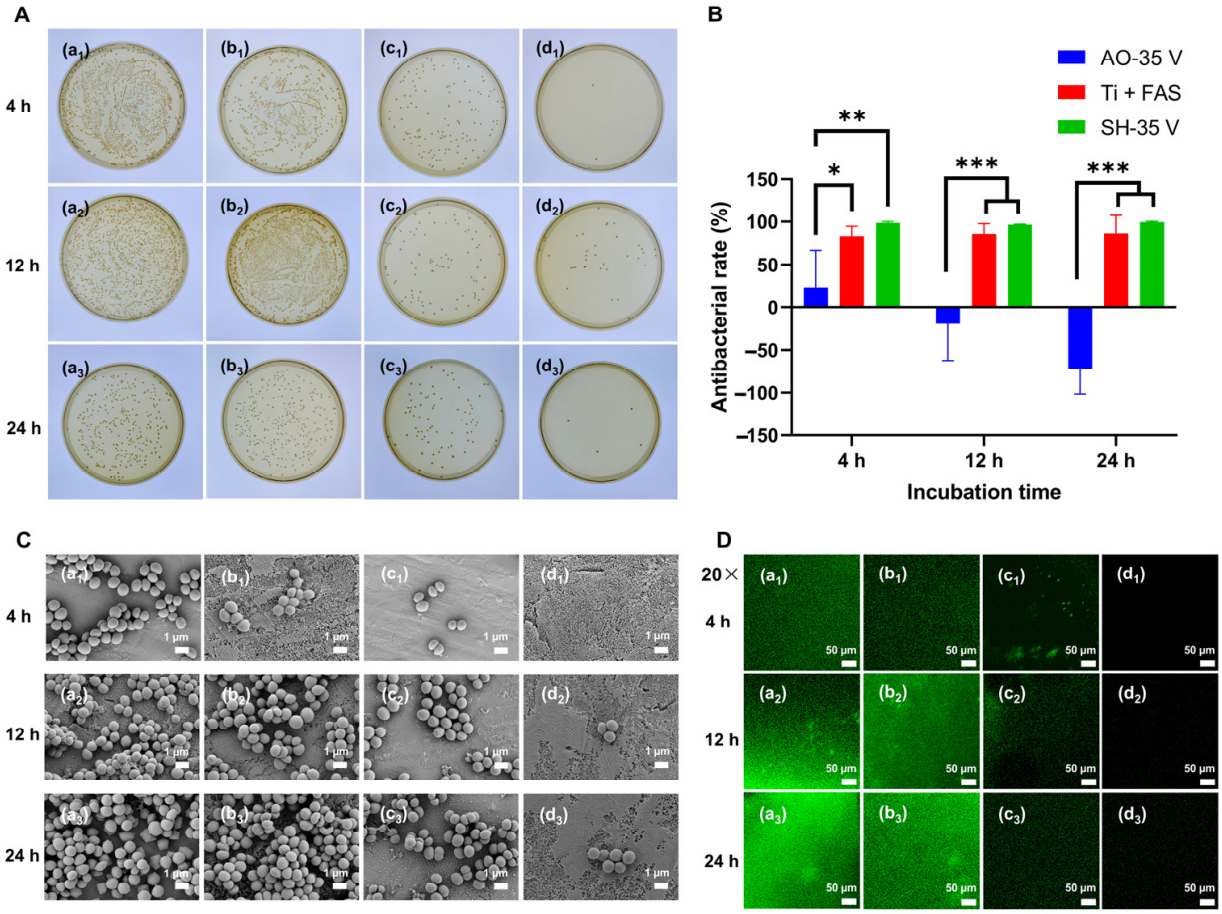

Figure 9. Evaluation of the antibacterial properties of different samples for *S. aureus*: (**A**) Colony counting, (**B**) antibacterial rate, and (**C**) SEM and (**D**) CLSM images on various sample surfaces. (**a_1–a_3**) Ti, (**b_1–b_3**) AO-35 V, (**c_1–c_3**) Ti + FAS, and (**d_1–d_3**) SH-35 V. All data are shown as mean ± standard deviation ($n \geq 3$) and assessed via two-way ANOVA; * $p < 0.05$, ** $p < 0.01$, *** $p < 0.001$.

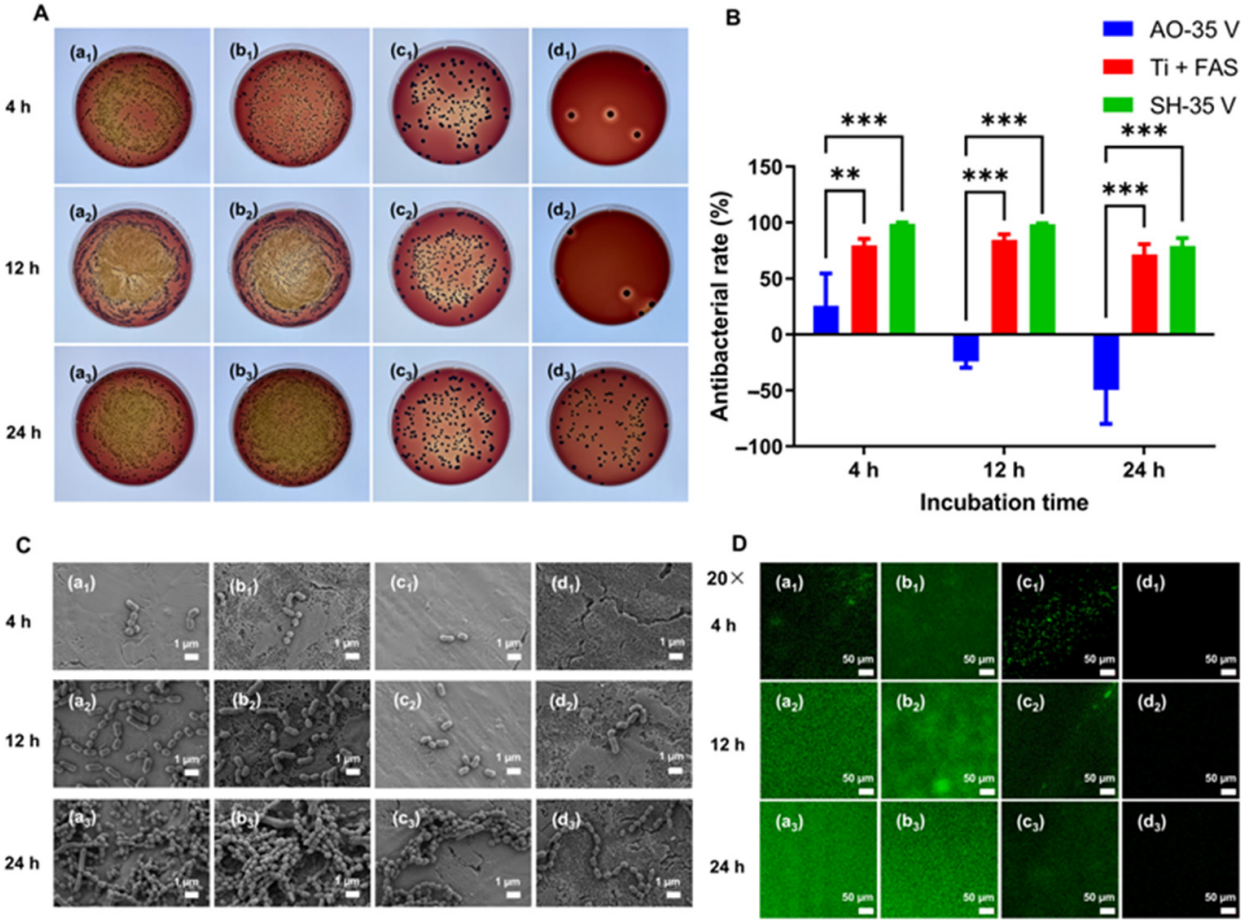

Figure 10. Evaluation of the antibacterial properties of different samples for *P.g*: (**A**) Colony counting, (**B**) antibacterial rate, and (**C**) SEM and (**D**) CLSM images on various sample surfaces. ($\mathbf{a_1}$–$\mathbf{a_3}$) Ti, ($\mathbf{b_1}$–$\mathbf{b_3}$) AO-35 V, ($\mathbf{c_1}$–$\mathbf{c_3}$) Ti + FAS, and ($\mathbf{d_1}$–$\mathbf{d_3}$) SH-35 V. All data are shown as mean ± standard deviation ($n \geq 3$) and assessed via two-way ANOVA; ** $p < 0.01$, *** $p < 0.001$.

3.4. Hemolytic and Anticoagulant Tests

Hemocompatibility is the most significant characteristic for blood-contact materials, so the inhibitory effect of hemolysis and thrombosis formation on the prepared Ti-based superhydrophobic coating surfaces was investigated [64]. As shown in Figure 11A, there was no statistically significant difference for Ti, AO-35 V, Ti + FAS, and SH-35 V, which were all lower than 5% and in accordance with the national standard for the hemolysis of implantable materials [52]. SH-35 V has the lowest hemolysis ratio of 1.1 ± 1% among all samples, indicating that the prepared Ti-based superhydrophobic coating has the most effectiveness to inhibit hemolysis. This could be ascribed to two main factors. First, the −OH on the TiO_2 surface is dehydrated and condensed with the −OH of FAS to form a strong chemical bonding combination, which can stabilize the pH value in the blood. Another important reason is that the superhydrophobic coating surface can trap large amounts of air to act as an air layer, thus further reducing the contact area between the blood and the coating. In such cases, the probability of the destruction of red blood cells was decreased, protecting the red blood cells from being destroyed. Blood coagulation, which is typically used as an indicator of hemocompatibility to assess biomaterials, is significantly influenced by platelet adhesion and activation [41]. Therefore, the static and dynamic anticoagulant properties were also evaluated in Figure 11B(a,b) and Figure 11B(c,d), respectively. Obviously, the majority of platelets adhered to the Ti surfaces, and the growth and dispersion of the dendritic extensions of adhered platelets could be easily observed, revealing that the adhered platelets were activated on the Ti substrate, as shown in Figure 11B(a). However,

no adhered platelets were observed on the SH-35 V surface as displayed in Figure 11B(b), which indicated that the SH-35 V surface can effectively resist platelet adhesion. In addition, due to the good results of the static anticoagulant test using fresh rabbit blood, whole blood from healthy adult volunteers was used for the dynamic anticoagulant test, which is closer to the actual implantation environment. As demonstrated in Figure 11B(c,d), the Ti surface exhibits dendritic extensions and more aggregation of the platelets as compared to SH-35 V. The above results exhibit that the SH-35 V coating can significantly reduce platelet adhesion and activation, and eventually prevent thrombosis, suggesting that SH-35 V offers superior anticoagulant properties, which in turn improves its hemocompatibility. The primary causes of this phenomenon are the rough TiO_2 nanotube structure and the entrapped air layer at the solid−blood interface, which can significantly reduce the direct contact area between the platelets and the superhydrophobic surface, resulting in decreasing platelet adhesion and deformation [65]. Moreover, the −OH on the Ti substrate is substituted by FAS molecules, lowering the surface polarity and further reducing the van der Waals force and hydrogen-bound interactions between the platelets and implant surface, which has an indirect effect on the coagulation mechanism [66].

3.5. Anticorrosion Test

The potentiodynamic polarization curves of bare Ti and SH-35 V were evaluated in artificial saliva in consideration of their dental application. The corrosion current density (J_{corr}) and corrosion potential (E_{corr}) were obtained using Tafel extrapolation. As is well known, a lower J_{corr} and a higher E_{corr} indicate greater corrosion resistance [67]. As demonstrated in Figure 12A and Table 2, the E_{corr} of the SH-35 V displays a significantly positive shift from −0.319 V to −0.214 V and the corresponding J_{corr} (6.427×10^{-9} A·cm^{-2}) is reduced by one order of magnitude as compared to that of bare Ti, suggesting its good corrosion inhibition. To further investigate the influence of corrosion on surface property, both the WCA and the surface morphology of different samples after the corrosion resistance test were evaluated. As shown in Figure 12B, the WCAs for both bare Ti and SH-35 V were decreased after the potentiodynamic polarization test. It can be seen that SH-35 V still remained highly hydrophobic with a WCA of 135.0 ± 3.4°, although it lost its superhydrophobicity. Figure 12C shows the SEM images of bare Ti and SH-35 V in artificial saliva before and after the potentiodynamic polarization test. It can be found that pitting corrosion occurred on bare Ti after the corrosion test (as indicated by red arrows in Figure 12b_1–b_3), while there was almost no morphology change for SH-35 V, indicating that the presence of our prepared SH-35 V could hinder the corrosive medium from reaching the bare Ti substrate in artificial saliva (pH = 7.0). All the above results prove that the as-prepared SH-35 V can protect the bare Ti effectively.

Table 2. The corrosion potential (E_{corr}) and corrosion current density (J_{corr}) of different samples.

Samples	E_{corr} (V vs. Ag/AgCl)	J_{corr} (A·cm^{-2})
Bare Ti	−0.319	1.698×10^{-8}
SH-35 V	−0.214	6.427×10^{-9}

The corrosion-inhibitive mechanism of the superhydrophobic surface is schematically shown in Figure 13. On the one hand, SH-35 V is composed of rough structures and modified by a low-surface-energy material, which can quickly trap large amounts of air within the pores in the coating. The entrapped air layer acts as a passivation layer and provides effective protection to the Ti substrate from being attacked by corrosive ions of Cl^- and PO_4^{3-} contained in the artificial saliva. Another key reason why the superhydrophobic coating can enhance the corrosion resistance of Ti substrate is "capillarity" [68]. The water can move easily against gravity in such a porous, rough structure when the CA of the surface is higher than 150°. As a result, the artificial saliva can be pushed out from the

pores of the superhydrophobic coating by the Laplace pressure and the Ti substrate can be greatly protected [69].

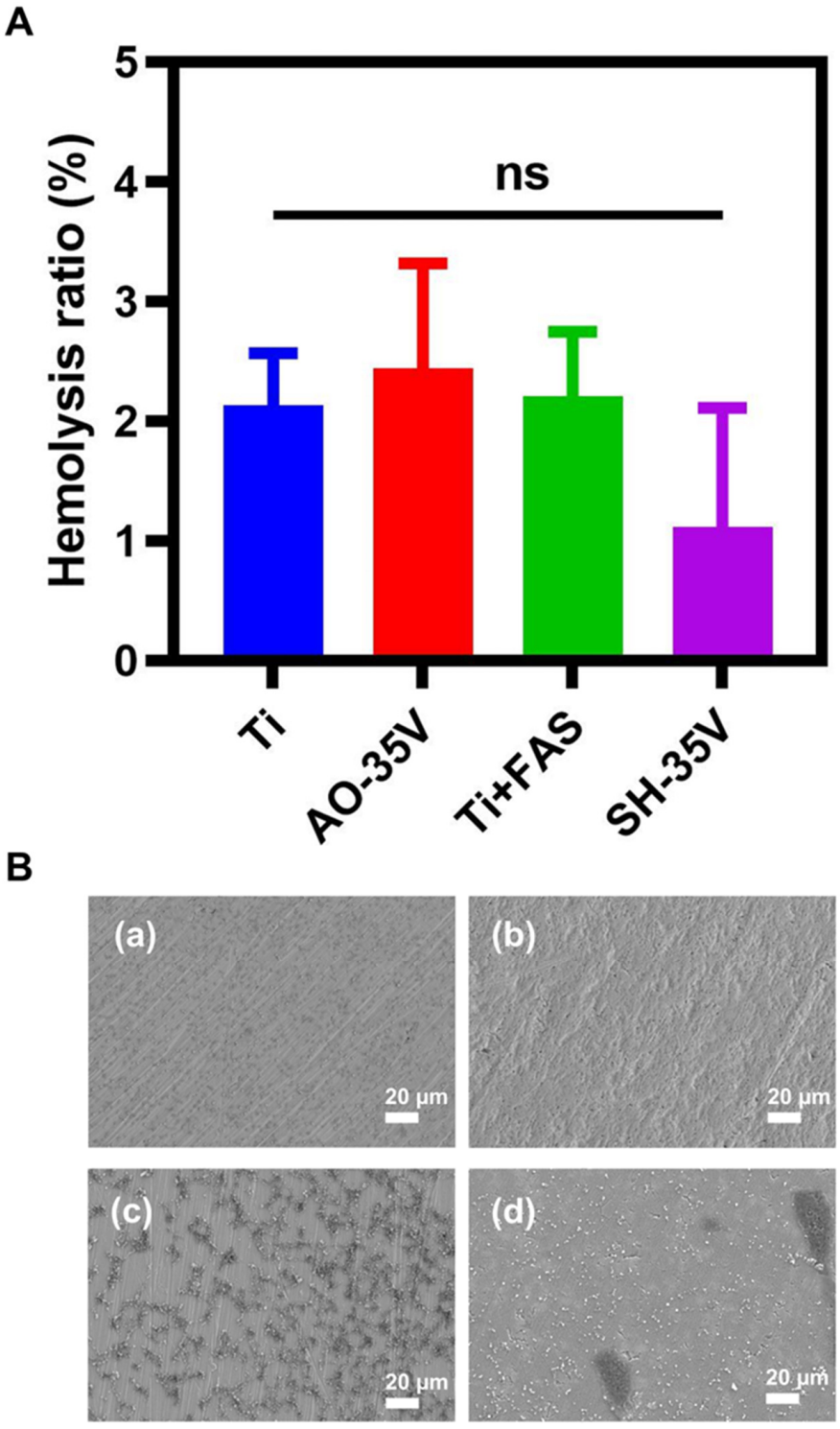

Figure 11. (**A**) Hemolysis ratio of different samples, and (**B**) evaluation of the static anticoagulant properties of (**a**) Ti and (**b**) SH-35 V and dynamic anticoagulant properties of (**c**) Ti and (**d**) SH-35 V.

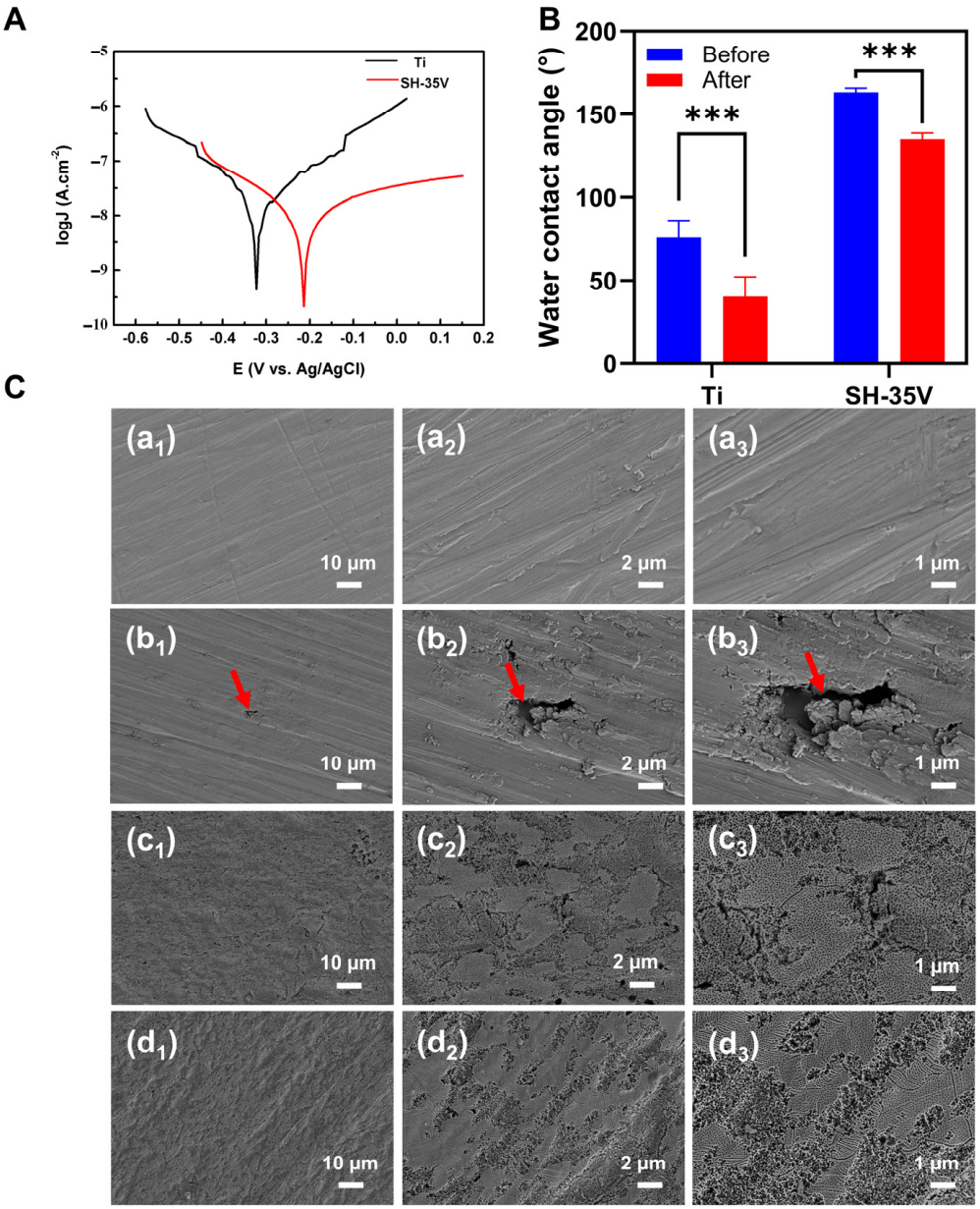

Figure 12. (**A**) Potentiodynamic polarization curves, and (**B**) WCA and (**C**) SEM images of bare Ti and SH-35 V before and after corrosion test in artificial saliva (pH = 7.0). (**a$_1$**–**a$_3$**) and (**c$_1$**–**c$_3$**) represent Ti and SH-35 V before corrosion test, respectively, (**b$_1$**–**b$_3$**) and (**d$_1$**–**d$_3$**) represent Ti and SH-35 V after corrosion test, respectively.

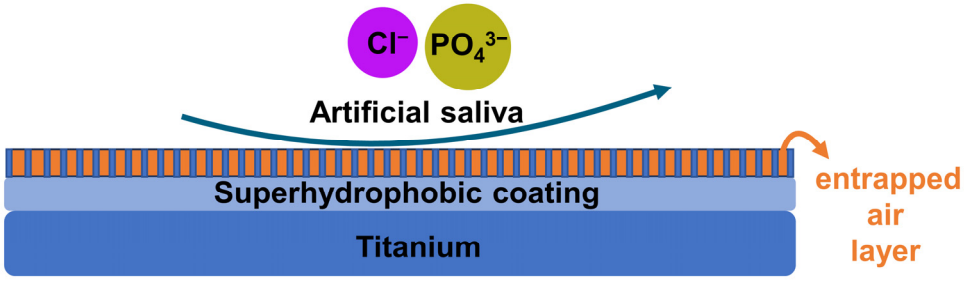

Figure 13. A schematic diagram of the corrosion resistance mechanism of superhydrophobic coating.

3.6. In Vivo Experiments

3.6.1. Abdominal Aortic Implantation

To further explore the anticoagulant possibilities in dental implant application, bare Ti and superhydrophobic Ti wires (SH-35 V) were implanted into the abdominal aorta of six- or eight-week-old SD rats for 1 h, respectively (Figure 14A). It can be observed that the bare Ti wire [Figure 14C(a_1,a_2)] and the superhydrophobic Ti wire [Figure 14C(b_1,b_2)] were clean and did not adhere to blood components before abdominal aortic implantation. After abdominal aortic implantation, the bare Ti wire was covered with more fibrin, dendritic extensions and aggregation of the platelets [as indicated by the yellow arrow in Figure 14C(a_4)], and erythrocytes [as indicated by the red arrow in Figure 14C(a_4)]. In contrast, no blood cell activation or aggregation can be observed on superhydrophobic Ti wire, as shown in Figure 14C(b_3,b_4). The superhydrophobic coating inhibits the adsorption of plasma proteins as well as the activation of the complement [70]. It also inhibits platelet adhesion and activation, thereby not triggering fibrin formation and deposition, and has excellent anticoagulant properties. The result *in vivo* is also in accordance with those of the static and dynamic anticoagulant tests *in vitro*, which indicated that the solid−blood interface still maintains the Cassie–Baxter state after abdominal aortic implantation for 1 h. In the Cassie–Baxter state, the rough structure of superhydrophobic Ti wire decreases the adhesion area with blood components [65,71]. Furthermore, FAS modification can reduce the surface polarity, resulting in a reduction in the van der Waals forces and hydrogen-bound interactions between the blood and the superhydrophobic Ti wire, which play a key role in the adhesion and activation of platelets on implantable materials [66].

3.6.2. Subcutaneous Implantation

The inflammatory reaction and tissue structure of the bare Ti rod and superhydrophobic Ti rod were assessed by subcutaneous implantation in six-week-old SD rats for 7, 15, and 28 days (Figure 14B). The results of a quantitative histological study are displayed in Figure 14D,E. As shown in Figure 14D(a_1–a_3,b_1–b_3), no noticeable inflammatory cell infiltration can be observed in either the bare Ti rod or the superhydrophobic Ti rod. To distinguish the structure and tissue components, Masson staining marked collagen as blue, and keratin and muscle fibers as red. As shown in Figure 14E(a_1–a_3,b_1–b_3), the subcutaneous tissue of the bare Ti rod and superhydrophobic Ti rod was normal with arranged collagen and muscle fibers. In addition, it has been reported that the thicker fibrous encapsulation is thought to indicate a more severe tissue response [72,73]. As shown in Figure 14D,E(a_1–a_3,b_1–b_3), the capsule around the bare Ti rod was thicker after implantation for 7, 15, and 28 days as compared to the superhydrophobic Ti rod. The bare Ti rod and the superhydrophobic Ti rod failed to produce any observable local tissue reactions or adverse consequences. The findings indicated that the superhydrophobic samples did not lead to serious inflammation, release harmful substances, or exhibit biologically incompatible surface chemistry. Moreover, superhydrophobic coatings are attractive candidates for preventing infection in implant sites due to their antibacterial qualities, which may reduce the first inflammation generated by microorganisms. The aforementioned results suggested that the superhydrophobic coating could effectively mitigate surface-induced infection.

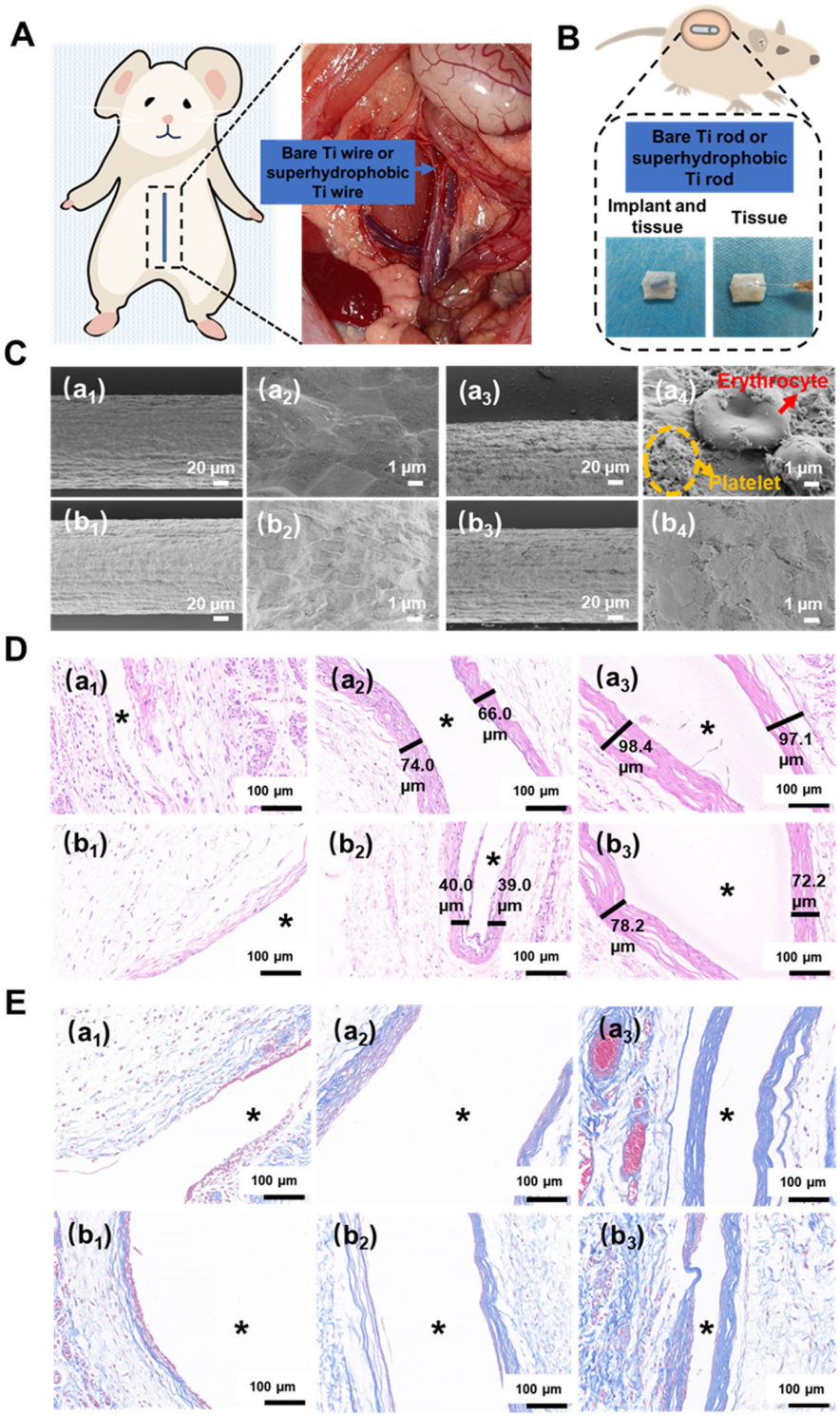

Figure 14. The illustrated diagram of (**A**) abdominal aortic implantation of bare Ti wire and superhydrophobic Ti wire; (**B**) subcutaneous implantation of bare Ti rod and superhydrophobic Ti rod; (**C**) SEM pictures of ($\mathbf{a_1}$,$\mathbf{a_2}$) bare Ti wire and ($\mathbf{b_1}$,$\mathbf{b_2}$) superhydrophobic Ti wire before implantation, and ($\mathbf{a_3}$,$\mathbf{a_4}$) bare Ti wire and ($\mathbf{b_3}$,$\mathbf{b_4}$) superhydrophobic Ti wire after abdominal aortic implantation for 1 h; (**D**) hematoxylin and eosin (HE) staining and (**E**) Masson staining of local tissue around ($\mathbf{a_1}$–$\mathbf{a_3}$) bare Ti rod and ($\mathbf{b_1}$–$\mathbf{b_3}$) superhydrophobic Ti rod samples after subcutaneous implantation for 7, 15, and 28 days. * represents the cavity after the Ti rod or superhydrophobic Ti rod has been removed.

4. Conclusions

In this study, a Ti-based superhydrophobic coating was fabricated via the combination of anodization and FAS modification, demonstrating improved antibacterial and anticoagulant properties, corrosion resistance, and good biocompatibility and biosafety. As a result, the thickness of the anodized samples is from 500 nm to 4 μm as the anodizing voltage increases. The Ti-based superhydrophobic coating demonstrated the existence of Ti, O, C, F, and Si elements, and the corresponding phase compositions are Ti and anatase. Additionally, the Ti-based superhydrophobic coating not only inhibits bacterial adhesion on the Ti substrate, which in turn decreases the likelihood of bacterial infections, but also reduces platelet adhesion and activation and eventually prevents thrombosis. Moreover, the as-prepared Ti-based superhydrophobic coating shows smaller J_{corr} and larger E_{corr}, indicating enhanced corrosion resistance, providing a promising strategy in dental applications such as dental implants, orthodontic brackets, orthodontic arch wires, and removable partial denture connectors.

Supplementary Materials: The following supporting information can be downloaded at https://www.mdpi.com/article/10.3390/coatings14050571/s1: Figure S1: Dynamic behavior of water droplets (5 μL) in contact with different sample surfaces. Sample A (a_1–a_5) and Sample B (b_1–b_5) represent the bare Ti and SH-35 V, respectively. The direction of the arrow indicates the movement direction of the needle tip; Figure S2: CA of artificial saliva on via anodization at different voltages for 1 h followed by FAS modification on coatings; Figure S3: The hydrophobicity of different kinds of liquids (10 μL) on SH-35 V; Figure S4: WCA of SH-35 V after storing at ambient temperature in air for 730 days; Figure S5: CA of artificial saliva on SH-35 V after storing at ambient temperature in air for 730 days; Figure S6: WCA of SH-35 V after immersion in artificial saliva for 2 days; Figure S7: CA of artificial saliva on SH-35 V after immersion in artificial saliva for 2 days; Figure S8: SEM images of anodized samples at different voltages: (a) AO-15 V, (b) AO-20 V, (c) AO-25 V, (d) AO-30 V, (e) AO-35 V, (f) AO-40 V, (g) AO-45 V, (h) AO-50 V, and (i) AO-55 V; Figure S9: SEM cross-sectional images of anodized samples at different voltages: (a) AO-15 V, (b) AO-20 V, (c) AO-25 V, (d) AO-30 V, (e) AO-35 V, (f) AO-40 V, (g) AO-45 V, (h) AO-50 V, and (i) AO-55 V; Figure S10: (a) SEM image and (b) SEM cross-sectional images of SH-35 V after immersion in artificial saliva for 2 days; Figure S11: EDS spectra of (a) bare Ti, (b) AO-35 V, (c) Ti + FAS, and (d) SH-35 V; Figure S12: XRD images of AO-35 V and SH-35 V. Video S1: A 5 μL water droplet is dropped onto Ti, demonstrating its hydrophilicity; Video S2: A 5 μL water droplet is dropped onto SH-35 V, exhibiting its low water adhesion; Video S3: The dynamic movement process of the water flow impinged onto SH-35V surface; Video S4: A mirror-like phenomenon appears when SH-35 V is immersed in water.

Author Contributions: Conceptualization, S.Z.; methodology, Q.R.; validation, S.Z.; formal analysis, Q.R., L.W. and J.Z.; investigation, Q.R., Y.C. (Yaqing Chen), Y.Y., D.L. and Y.D.; resources, S.Z.; writing—original draft, S.Z. and Q.R.; writing—review and editing, S.Z., Y.C. (Ying Cao), J.C., X.L., Q.R., H.Q. and Q.L.; supervision, S.Z.; project administration, S.Z.; funding acquisition, S.Z. All authors have read and agreed to the published version of the manuscript.

Funding: This work was funded by the National Natural Science Foundation of China (grant no. 82101070); the Key Research and Development Program of Anhui Province (grant no. 2022e07020051); the College Young and Middle-Aged Teachers Training Action Project of Anhui Education Department (YQZD2023024); the Anhui Province Translational Medical College Research Fund Project (grant no. 2021zhyxC51); the Natural Science Foundation of Anhui Province (grant no. 2008085QH374); the Anhui Medical University Basic and Clinical Collaborative Research Enhancement Program (2019xkjT019); Grants for Scientific Research of BSKY (grant no. XJ201918) from Anhui Medical University; 2022 Disciplinary Construction Project in the School of Dentistry, Anhui Medical University (grant no. 2022xkfyts09); the 2021 Disciplinary Construction Project in the School of Dentistry, Anhui Medical University (grant no. 2021kqxkFY17); and the Research Improvement Program of Stomatologic Hospital & College of Anhui Medical University (grant no. 2020kqkyT02).

Institutional Review Board Statement: This study was conducted in accordance with the Declaration of Helsinki, and approved by the Ethics Committee of Anhui Medical University (protocol code: S 20200048; date of approval: 2 August 2019). The animal study protocol was approved by the Ethics

Committee of Anhui Medical University (protocol code: LLSC20190702; date of approval: 2 August 2019).

Informed Consent Statement: Not applicable.

Data Availability Statement: All data from the study are contained in this paper and its supporting information.

Conflicts of Interest: The authors declare no conflicts of interest.

References

1. Spriano, S.; Yamaguchi, S.; Baino, F.; Ferraris, S. A critical review of multifunctional titanium surfaces: New frontiers for improving osseointegration and host response, avoiding bacteria contamination. *Acta Biomater.* **2018**, *79*, 1–22. [CrossRef] [PubMed]
2. Kaur, M.; Singh, K. Review on titanium and titanium based alloys as biomaterials for orthopaedic applications. *Mater. Sci. Eng. C* **2019**, *102*, 844–862. [CrossRef] [PubMed]
3. Valiev, R.Z.; Semenova, I.P.; Latysh, V.V.; Rack, H.; Lowe, T.C.; Petruzelka, J.; Dluhos, L.; Hrusak, D.; Sochova, J. Nanostructured Titanium for Biomedical Applications. *Adv. Eng. Mater.* **2008**, *10*, 1–4. [CrossRef]
4. Miyazaki, S.; Kim, H.Y.; Hosoda, H. Development and characterization of Ni-free Ti-base shape memory and superelastic alloys. *Mater. Sci. Eng. A* **2006**, *438–440*, 18–24. [CrossRef]
5. Sheremetyev, V.; Petrzhik, M.; Zhukova, Y.; Kazakbiev, A.; Arkhipova, A.; Moisenovich, M.; Prokoshkin, S.; Brailovski, V. Structural, physical, chemical, and biological surface characterization of thermomechanically treated Ti-Nb-based alloys for bone implants. *J. Biomed. Mater. Res.* **2019**, *108B*, 647–662. [CrossRef] [PubMed]
6. Geetha, M.; Singh, A.K.; Asokamani, R.; Gogia, A.K. Ti based biomaterials, the ultimate choice for orthopaedic implants—A review. *Prog. Mater. Sci.* **2009**, *54*, 397–425. [CrossRef]
7. Rossiter, S.E.; Fletcher, M.H.; Wuest, W.M. Natural products as platforms to overcome antibiotic resistance. *Chem. Rev.* **2017**, *117*, 12415–12474. [CrossRef] [PubMed]
8. Laxminarayan, R.; Duse, A.; Wattal, C.; Zaidi, A.K.; Wertheim, H.F.; Sumpradit, N.; Vlieghe, E.; Hara, G.L.; Gould, I.M.; Goossens, H.; et al. Antibiotic resistance-the need for global solutions. *Lancet Infect. Dis.* **2013**, *13*, 1057–1098. [CrossRef] [PubMed]
9. Li, X.; Bai, H.; Yang, Y.; Yoon, J.; Wang, S.; Zhang, X. Supramolecular antibacterial materials for combatting antibiotic resistance. *Adv. Mater.* **2019**, *31*, e1805092. [CrossRef]
10. Knetsch, M.L.W.; Koole, L.H. New strategies in the development of antimicrobial coatings: The example of increasing usage of silver and silver nanoparticles. *Polymers* **2011**, *3*, 340–366. [CrossRef]
11. Zhang, E.; Zhao, X.; Hu, J.; Wang, R.; Fu, S.; Qin, G. Antibacterial metals and alloys for potential biomedical implants. *Bioact. Mater.* **2021**, *6*, 2569–2612. [CrossRef] [PubMed]
12. Rao, Q.; Weng, L.; Zhang, J.; Liu, D.; Zhang, W.; Chen, S.; Chen, J.; Li, X.; Qiu, H.; Cao, Y.; et al. Research progress in superhydrophobic titanium-based implants for antibacterial applications. *Coatings* **2023**, *13*, 419. [CrossRef]
13. Inzana, J.A.; Schwarz, E.M.; Kates, S.L.; Awad, H.A. Biomaterials approaches to treating implant-associated osteomyelitis. *Biomaterials* **2016**, *81*, 58–71. [CrossRef] [PubMed]
14. Jokinen, V.; Kankuri, E.; Hoshian, S.; Franssila, S.; Ras, R.H.A. Superhydrophobic blood-repellent surfaces. *Adv. Mater.* **2018**, *30*, 1705104. [CrossRef] [PubMed]
15. Zhang, X.; Wan, Y.; Ren, B.; Wang, H.; Yu, M.; Liu, A.; Liu, Z. Preparation of superhydrophobic surface on titanium alloy via micro-milling, anodic oxidation and fluorination. *Micromachines* **2020**, *11*, 316. [CrossRef] [PubMed]
16. Gorbet, M.B.; Sefton, M.V. Biomaterial-associated thrombosis: Roles of coagulation factors, complement, platelets and leukocytes. *Biomaterials* **2004**, *25*, 5681–5703. [CrossRef] [PubMed]
17. Mystkowska, J.; Niemirowicz-Laskowska, K.; Łysik, D.; Tokajuk, G.; Dąbrowski, J.; Bucki, R. The role of oral cavity biofilm on metallic biomaterial surface destruction–corrosion and friction aspects. *Int. J. Mol. Sci.* **2018**, *19*, 743. [CrossRef] [PubMed]
18. Siddiqui, D.A.; Guida, L.; Sridhar, S.; Valderrama, P.; Wilson, T.G.; Rodrigues, D.C. Evaluation of oral microbial corrosion on the surface degradation of dental implant materials. *J. Periodontol.* **2018**, *90*, 72–81. [CrossRef] [PubMed]
19. Rafieerad, A.R.; Bushroa, A.R.; Zalnezhad, E.; Sarraf, M.; Basirun, W.J.; Baradaran, S.; Nasiri-Tabrizi, B. Microstructural development and corrosion behavior of self-organized TiO_2 nanotubes coated on Ti–6Al–7Nb. *Ceram. Int.* **2015**, *41*, 10844–10855. [CrossRef]
20. Schutzius, T.M.; Jung, S.; Maitra, T.; Graeber, G.; Kohme, M.; Poulikakos, D. Spontaneous droplet trampolining on rigid superhydrophobic surfaces. *Nature* **2015**, *527*, 82–85. [CrossRef] [PubMed]
21. Peng, C.; Chen, Z.; Tiwari, M.K. All-organic superhydrophobic coatings with mechanochemical robustness and liquid impalement resistance. *Nat. Mater.* **2018**, *17*, 355–360. [CrossRef] [PubMed]
22. Zheng, S.; Li, C.; Zhang, Y.; Xiang, T.; Cao, Y.; Li, Q.; Chen, Z. A general strategy towards superhydrophobic self-cleaning and anti-corrosion metallic surfaces: An example with aluminum alloy. *Coatings* **2021**, *11*, 788. [CrossRef]
23. Zheng, S.; Bellido-Aguilar, D.A.; Huang, Y.; Zeng, X.; Zhang, Q.; Chen, Z. Mechanically robust hydrophobic bio-based epoxy coatings for anti-corrosion application. *Surf. Coat. Technol.* **2019**, *363*, 43–50. [CrossRef]

24. Wang, L.; Gong, Q.; Zhan, S.; Jiang, L.; Zheng, Y. Robust anti-icing performance of a flexible superhydrophobic surface. *Adv. Mater.* **2016**, *28*, 7729–7735. [CrossRef] [PubMed]
25. Shen, Y.; Wang, G.; Tao, J.; Zhu, C.; Liu, S.; Jin, M.; Xie, Y.; Chen, Z. Anti-icing performance of superhydrophobic texture surfaces depending on reference environments. *Adv. Mater. Interfaces* **2017**, *4*, 1700836. [CrossRef]
26. Gao, S.; Dong, X.; Huang, J.; Li, S.; Li, Y.; Chen, Z.; Lai, Y. Rational construction of highly transparent superhydrophobic coatings based on a non-particle, fluorine-free and water-rich system for versatile oil-water separation. *Chem. Eng. J.* **2018**, *333*, 621–629. [CrossRef]
27. Fu, Q.; Wu, X.; Kumar, D.; Ho, J.W.; Kanhere, P.D.; Srikanth, N.; Liu, E.; Wilson, P.; Chen, Z. Development of sol-gel icephobic coatings: Effect of surface roughness and surface energy. *ACS Appl. Mater. Interfaces* **2014**, *6*, 20685–20692. [CrossRef] [PubMed]
28. Jaiswal, S.; McHale, P.; Duffy, B. Preparation and rapid analysis of antibacterial silver, copper and zinc doped sol-gel surfaces. *Colloids Surf. B* **2012**, *94*, 170–176. [CrossRef]
29. Gao, X.; Tong, W.; Ouyang, X.; Wang, X. Facile fabrication of a superhydrophobic titanium surface with mechanical durability by chemical etching. *RSC Adv.* **2015**, *5*, 84666–84672. [CrossRef]
30. Dong, C.; Gu, Y.; Zhong, M.; Li, L.; Sezer, K.; Ma, M.; Liu, W. Fabrication of superhydrophobic Cu surfaces with tunable regular micro and random nano-scale structures by hybrid laser texture and chemical etching. *J. Mater. Process. Technol.* **2011**, *211*, 1234–1240. [CrossRef]
31. Li, J.; Jing, Z.; Yang, Y.; Wang, Q.; Lei, Z. From Cassie state to Gecko state: A facile hydrothermal process for the fabrication of superhydrophobic surfaces with controlled sliding angles on zinc substrates. *Surf. Coat. Technol.* **2014**, *258*, 973–978. [CrossRef]
32. Wang, B.; Wu, Z.; Lan, J.; Li, Y.; Xie, L.; Huang, X.; Zhang, A.; Qiao, H.; Chang, X.; Lin, H.; et al. Surface modification of titanium implants by silk fibroin/Ag co-functionalized strontium titanate nanotubes for inhibition of bacterial-associated infection and enhancement of *in vivo* osseointegration. *Surf. Coat. Technol.* **2021**, *405*, 126700. [CrossRef]
33. Ganesh, V.A.; Nair, A.S.; Raut, H.K.; Yuan Tan, T.T.; He, C.; Ramakrishna, S.; Xu, J. Superhydrophobic fluorinated POSS–PVDF-HFP nanocomposite coating on glass by electrospinning. *J. Mater. Chem.* **2012**, *22*, 18479–18485. [CrossRef]
34. Roy, M.; Bandyopadhyay, A.; Bose, S. Induction plasma sprayed nano hydroxyapatite coatings on titanium for orthopaedic and dental implants. *Surf. Coat. Technol.* **2011**, *205*, 2785–2792. [CrossRef] [PubMed]
35. Jeong, C.; Choi, C.H. Single-step direct fabrication of pillar-on-pore hybrid nanostructures in anodizing aluminum for superior superhydrophobic efficiency. *ACS Appl. Mater. Interfaces* **2012**, *4*, 842–848. [CrossRef] [PubMed]
36. Zong, M.; Bai, L.; Liu, Y.; Wang, X.; Zhang, X.; Huang, X.; Hang, R.; Tang, B. Antibacterial ability and angiogenic activity of Cu-Ti-O nanotube arrays. *Mater. Sci. Eng. C* **2017**, *71*, 93–99. [CrossRef] [PubMed]
37. Souza, J.G.S.; Bertolini, M.; Costa, R.C.; Cordeiro, J.M.; Nagay, B.E.; de Almeida, A.B.; Retamal-Valdes, B.; Nociti, F.H.; Feres, M.; Rangel, E.C.; et al. Targeting pathogenic biofilms: Newly developed superhydrophobic coating favors a host-compatible microbial profile on the titanium surface. *ACS Appl. Mater. Interfaces* **2020**, *12*, 10118–10129. [CrossRef] [PubMed]
38. Tang, P.; Zhang, W.; Wang, Y.; Zhang, B.; Wang, H.; Lin, C.; Zhang, L. Effect of superhydrophobic surface of titanium on *Staphylococcus aureus* adhesion. *J. Nanomater.* **2011**, *2011*, 178921. [CrossRef]
39. Bartlet, K.; Movafaghi, S.; Dasi, L.P.; Kota, A.K.; Popat, K.C. Antibacterial activity on superhydrophobic titania nanotube arrays. *Colloids Surf. B* **2018**, *166*, 179–186. [CrossRef] [PubMed]
40. Montgomerie, Z.; Popat, K.C. Improved hemocompatibility and reduced bacterial adhesion on superhydrophobic titania nanoflower surfaces. *Mater. Sci. Eng. C* **2021**, *119*, 111503. [CrossRef] [PubMed]
41. Zhang, J.; Li, G.; Li, D.; Zhang, X.; Li, Q.; Liu, Z.; Fang, Y.; Zhang, S.; Man, J. *In vivo* blood-repellent performance of a controllable facile-generated superhydrophobic surface. *ACS Appl. Mater. Interfaces* **2021**, *13*, 29021–29033. [CrossRef] [PubMed]
42. Yang, C.; Cao, W.; Yang, Z.; Wang, M.; Jing, X.; Tian, Y. The study on the anti-corrosion performance of NiTi alloy in human body solution with the fabricating processes of laser irradiation and PDMS modification. *J. Bionic Eng.* **2021**, *18*, 77–91. [CrossRef]
43. Bartlet, K.; Movafaghi, S.; Kota, A.; Popat, K.C. Superhemophobic titania nanotube array surfaces for blood contacting medical devices. *RSC Adv.* **2017**, *7*, 35466–35476. [CrossRef]
44. Sabino, R.M.; Kauk, K.; Movafaghi, S.; Kota, A.; Popat, K.C. Interaction of blood plasma proteins with superhemophobic titania nanotube surfaces. *Nanomedicine* **2019**, *21*, 102046. [CrossRef] [PubMed]
45. Deng, R.; Hu, Y.M.; Wang, L.; Li, Z.H.; Shen, T.; Zhu, Y.; Xiang, J.Z. An easy and environmentally-friendly approach to superamphiphobicity of aluminum surfaces. *Appl. Surf. Sci.* **2017**, *402*, 301–307. [CrossRef]
46. Tudu, B.K.; Sinhamahapatra, A.; Kumar, A. Surface Modification of Cotton Fabric Using TiO_2 Nanoparticles for Self-Cleaning, Oil–Water Separation, Antistain, Anti-Water Absorption, and Antibacterial Properties. *ACS Omega* **2020**, *5*, 7850–7860. [CrossRef] [PubMed]
47. Burton, Z.; Bhushan, B. Hydrophobicity, Adhesion, and Friction Properties of Nanopatterned Polymers and Scale Dependence for Micro- and Nanoelectromechanical Systems. *Nano Lett.* **2005**, *5*, 1607–1613. [CrossRef]
48. Falde, E.J.; Yohe, S.T.; Colson, Y.L.; Grinstaff, M.W. Superhydrophobic materials for biomedical applications. *Biomaterials* **2016**, *104*, 87–103. [CrossRef] [PubMed]
49. Wang, X.; Xu, K.; Cui, W.; Yang, X.; Maitz, M.F.; Li, W.; Li, X.; Chen, J. Controlled synthesis of mussel-inspired Ag nanoparticle coatings with demonstrated *in vitro* and *in vivo* antibacterial properties. *Mater. Des.* **2021**, *208*, 109944. [CrossRef]
50. Li, Y.; Ma, Y.; Yu, J.; Li, C.; Yu, D.; Dai, R.; Li, Q.; Cao, C.Y. A dual functional polypeptide with antibacterial and anti-inflammatory properties for the treatment of periodontitis. *Int. J. Biol. Macromol.* **2023**, *242*, 124920. [CrossRef] [PubMed]

51. Lafaurie, G.I.; Sabogal, M.A.; Castillo, D.M.; Rincón, M.V.; Gómez, L.A.; Lesmes, Y.A.; Chambrone, L. Microbiome and microbial biofilm profiles of peri-implantitis: A systematic review. *J. Periodontol.* **2017**, *88*, 1066–1089. [CrossRef] [PubMed]
52. Chen, Y.; Wan, G.; Wang, J.; Zhao, S.; Zhao, Y.; Huang, N. Covalent immobilization of phytic acid on Mg by alkaline pre-treatment: Corrosion and degradation behavior in phosphate buffered saline. *Corros. Sci.* **2013**, *75*, 280–286. [CrossRef]
53. Peng, S.; Tian, D.; Yang, X.; Deng, W. Highly efficient and large-scale fabrication of superhydrophobic alumina surface with strong stability based on self-congregated alumina nanowires. *ACS Appl. Mater. Interfaces* **2014**, *6*, 4831–4841. [CrossRef] [PubMed]
54. Liu, J.; Liu, H.; Yang, X.; Jia, X.; Cai, M.; Bao, Y. Preparation of Si–Mn/biochar composite and discussions about characterizations, advances in application and adsorption mechanisms. *Chemosphere* **2021**, *281*, 130946. [CrossRef] [PubMed]
55. Zhang, K.; Huang, J.; Yu, G.; Zhang, Q.; Deng, S.; Wang, B. Destruction of perfluorooctane sulfonate (PFOS) and perfluorooctanoic acid (PFOA) by ball milling. *Environ. Sci. Technol.* **2013**, *47*, 6471–6477. [CrossRef] [PubMed]
56. Alban, L.; Monteiro, W.F.; Diz, F.M.; Miranda, G.M.; Scheid, C.M.; Zotti, E.R.; Morrone, F.B.; Ligabue, R. New quercetin-coated titanate nanotubes and their radiosensitization effect on human bladder cancer. *Mater. Sci. Eng. C* **2020**, *110*, 110662. [CrossRef] [PubMed]
57. Jiang, J.Y.; Xu, J.L.; Liu, Z.H.; Deng, L.; Sun, B.; Liu, S.D.; Wang, L.; Liu, H.Y. Preparation, corrosion resistance and hemocompatibility of the superhydrophobic TiO_2 coatings on biomedical Ti-6Al-4V alloys. *Appl. Surf. Sci.* **2015**, *347*, 591–595. [CrossRef]
58. Huang, J.; Lai, Y.; Wang, L.; Li, S.; Ge, M.; Zhang, K.; Fuchs, H.; Chi, L. Controllable wettability and adhesion on bioinspired multifunctional TiO_2 nanostructure surfaces for liquid manipulation. *J. Mater. Chem. A* **2014**, *2*, 18531–18538. [CrossRef]
59. Sorkin, J.A.; Hughes, S.; Soares, P.; Popat, K.C. Titania nanotube arrays as interfaces for neural prostheses. *Mater. Sci. Eng. C* **2015**, *49*, 735–745. [CrossRef] [PubMed]
60. Zhao, S.; Yang, X.; Xu, Y.; Weng, Z.; Liao, L.; Wang, X. A sprayable superhydrophobic dental protectant with photo-responsive anti-bacterial, acid-resistant, and anti-fouling functions. *Nano Res.* **2022**, *15*, 5245–5255. [CrossRef]
61. Mei, S.; Wang, H.; Wang, W.; Tong, L.; Pan, H.; Ruan, C.; Ma, Q.; Liu, M.; Yang, H.; Zhang, L.; et al. Antibacterial effects and biocompatibility of titanium surfaces with graded silver incorporation in titania nanotubes. *Biomaterials* **2014**, *35*, 4255–4265. [CrossRef] [PubMed]
62. Neufeld, B.H.; Reynolds, M.M. Critical nitric oxide concentration for *Pseudomonas aeruginosa* biofilm reduction on polyurethane substrates. *Biointerphases* **2016**, *11*, 031012. [CrossRef] [PubMed]
63. Fadeeva, E.; Truong, V.K.; Stiesch, M.; Chichkov, B.N.; Crawford, R.J.; Wang, J.; Ivanova, E.P. Bacterial retention on superhydrophobic titanium surfaces fabricated by femtosecond laser ablation. *Langmuir* **2011**, *27*, 3012–3019. [CrossRef] [PubMed]
64. Zhao, Q.; Fan, Y.; Zhang, Y.; Liu, J.; Li, W.; Weng, Y. Copper-based SURMOFs for nitric oxide generation: Hemocompatibility, vascular cell growth, and tissue response. *ACS Appl. Mater. Interfaces* **2019**, *11*, 7872–7883. [CrossRef] [PubMed]
65. Movafaghi, S.; Leszczak, V.; Wang, W.; Sorkin, J.A.; Dasi, L.P.; Popat, K.C.; Kota, A.K. Hemocompatibility of Superhemophobic Titania Surfaces. *Adv. Healthc. Mater.* **2016**, *6*, 1600717. [CrossRef] [PubMed]
66. Yang, Y.; Lai, Y.; Zhang, Q.; Wu, K.; Zhang, L.; Lin, C.; Tang, P. A novel electrochemical strategy for improving blood compatibility of titanium-based biomaterials. *Colloids Surf. B* **2010**, *79*, 309–313. [CrossRef] [PubMed]
67. Tian, P.; Zhao, X.; Sun, B.; Cao, H.; Zhao, Y.; Yan, J.; Xue, Y.; Lin, H.; Han, S.; Ren, T.; et al. Enhanced anticorrosion and tribological properties of Ti6Al4V alloys with Fe_3O_4/HA coatings. *Surf. Coat. Technol.* **2022**, *433*, 128118. [CrossRef]
68. Zheng, S.; Li, C.; Fu, Q.; Li, M.; Hu, W.; Wang, Q.; Du, M.; Liu, X.; Chen, Z. Fabrication of self-cleaning superhydrophobic surface on aluminum alloys with excellent corrosion resistance. *Surf. Coat. Technol.* **2015**, *276*, 341–348. [CrossRef]
69. Mohamed, A.M.A.; Abdullah, A.M.; Younan, N.A. Corrosion behavior of superhydrophobic surfaces: A review. *Arab. J. Chem.* **2015**, *8*, 749–765. [CrossRef]
70. Yu, H.; Qiu, H.; Ma, W.; Maitz, M.F.; Tu, Q.; Xiong, K.; Chen, J.; Huang, N.; Yang, Z. Endothelium-mimicking surface combats thrombosis and biofouling via synergistic long- and short-distance defense strategy. *Small* **2021**, *17*, 2100729. [CrossRef] [PubMed]
71. Moradi, S.; Hadjesfandiari, N.; Toosi, S.F.; Kizhakkedathu, J.N.; Hatzikiriakos, S.G. Effect of Extreme Wettability on Platelet Adhesion on Metallic Implants: From Superhydrophilicity to Superhydrophobicity. *ACS Appl. Mater. Interfaces* **2016**, *8*, 17631–17641. [CrossRef] [PubMed]
72. Anderson, J.M.; Rodriguez, A.; Chang, D.T. Foreign body reaction to biomaterials. *Semin. Immunol.* **2008**, *20*, 86–100. [CrossRef] [PubMed]
73. Avula, M.N.; Rao, A.N.; McGill, L.D.; Grainger, D.W.; Solzbacher, F. Foreign body response to subcutaneous biomaterial implants in a mast cell-deficient $Kit^{w\text{-}Sh}$ murine model. *Acta Biomater.* **2014**, *10*, 1856–1863. [CrossRef] [PubMed]